이학석사 학위논문

Molecular Dynamics Studies on SARS-CoV-2 Neutralizing Antibodies and Kynureninases

SARS-CoV-2 중화 항체와 키누레닌 효소에 대한 분자 동역학 연구

2023년 8월

서울대학교 대학원

화학부 물리화학 전공

이 지 현

Molecular Dynamics Studies on SARS-CoV-2 Neutralizing Antibodies and Kynureninases

지도 교수 석 차 옥

이 논문을 이학석사 학위논문으로 제출함

2023년 7월

서울대학교 대학원
화학부 물리화학 전공
이 지 현

이지현의 이학석사 학위논문을 인준함
2023년 7월

위 원 장 신석민 (인)

부위원장 석차옥 (인)

위 원 정연준 (인)

ABSTRACT

Molecular Dynamics Studies on SARS-CoV-2 Neutralizing Antibodies and Kynureninases

Jihyeon Lee
Department of Chemistry
The Graduate School
Seoul National University

The dynamic role of proteins *in vivo* has become perceived increasingly important in the field of therapeutics. Therapeutic proteins possess specific functions that contribute to disease alleviation when they interact with specific disease target molecules: invoking immune responses, catalyzing biochemical reactions, transporting molecules, and assembling into membranes without interfering with other biological pathways. However, limited understanding of protein-protein and protein-ligand interactions still hinders effective development of protein therapeutics.

In this thesis, molecular interactions occurring in functional proteins, such as antibodies and enzymes, are investigated with a focus on binding thermodynamics and kinetics, respectively. This is achieved through atomic-level molecular dynamics simulations and

statistical analysis of residue-wise binding free energies and residence times. First, the simultaneous formation of multiple contacts between antibodies and their target proteins (SARS-CoV-2 RBD) was observed to contributes to favorable binding affinity. Second, **π**-interactions, facilitated by hydrogen bonds formed between residues in enzyme and its substrate, was found to stabilize the binding pose and to improve binding kinetics upon substrate binding, resulting in longer residence times. These studies provide enhanced understanding of detailed atomic contributions in molecular interactions of therapeutic proteins and hence, new strategies for improved design of protein therapeutics.

Keywords: molecular dynamics simulation, binding thermodynamics, solvation free energy, binding kinetics, residence time, protein therapeutics

Student Number: *2021-26772*

TABLE OF CONTENTS

LIST OF FIGURES

LIST OF TABLES

1. INTRODUCTION

Therapeutic proteins should possess specific functions for disease alleviation *in vivo* when they interact with the biological systems. The functional proteins are responsible for invoking immune responses, catalyzing biochemical reactions, transporting molecular building blocks, and assembling into membranes without interfering with other biological pathways. (Keskin et al., 2008, Zhu et al., 2021) Therefore, understanding molecular interactions in the level of protein-protein and protein-ligand complex has gained significant imporatnce in the field of protein therapeutics since it provides the essential information on their function and efficient ways to design them. (Sudha et al., 2014, Lu et al., 2020) However, clear understanding of which specific interactions help a functional protein gain its function requires detailed atomistic study.

Molecular dynamics (MD) simulation is a critical tool for exploring the biological mechanisms in atomic detail occurring by explicitly considering molecular interactions in protein-protein and protein-ligand complexes. (Karplus et al., 2002) Although there have been significant efforts to quantify the binding thermodynamics and kinetics with MD simulations, those methods still need to be improved in accuracy. (Gromiha et al., 2017) For example, binding free energy, or the binding affinity can be calculated based on the free energy perturbation and thermodynamic integration methods. (Deng et al., 2009) However, these methods are limited to free energy changes involving only small changes from the reference systems and thus are not proper for evaluating binding free energy.

To overcome the sampling problem, machine learning approaches have been introduced to predict the binding affinity. (Bernetti, M. et al., 2020) Even though they can provide results in a relatively short time as a linear expression of energy function with a high prediction accuracy (Bertazzo, M. et al., 2021, Vreven, T. et al., 2012), they need to be improved to get higher level of accuracy to describe the precise nature of interactions on unseen data. Furthermore, computing residence time is one of the most direct methodologies for calculating and predicting kinetics of receptor-ligand complex. (Kokh et al., 2018) However, the development of well-established strategies to quantify the effectiveness of ligand-receptor interaction kinetics requires molecular kinetics studies. (Bernetti, M. et al., 2019)

Here, we explore how to find key interactions combined with MD simulations in terms of binding thermodynamics and kinetics on two classes of therapeutic proteins, SARS-CoV-2 neutralizing antibodies in Chapter 2 and therapeutic enzymes in Chapter 3. In **Chapter 2**, we suggest the role of simultaneous multiple contacts in alleviating dehydration penalty and making favorable binding free energies between antigen and antibody proteins. We analyze them by applying residue decomposition solvation free energy calculation without any structural perturbation. In **Chapter 3**, we provide an advanced understanding on different binding kinetics between human kynureninase (HsKYNU) and pseudomonas kynureninase (PfKYNU) which are relevant to humanized cancer therapy. We propose the difference in binding kinetics between the two enzymes and quantify substrates' residence time in enzymes by calculating hydrogen bond populations.

2. Atomic-level thermodynamic analysis of the binding free energy of SARS-CoV-2 neutralizing antibodies

2.1. Introduction

Understanding protein-protein interactions (PPIs) in the atomic level is widely acknowledged as crucial in the field of protein therapeutics development. Investigating PPIs provides valuable insights into the biological mechanisms associated with various diseases and drug strategies. (Arkin et al., 2004, Smith et al., 2012, Petta et al., 2016) However, our current understanding of the individual molecular interactions that occur between interfacial amino acids and contribute to build up PPIs, as well as their role in determining binding affinity remains incomplete and limited. (Scott et al., 2016, Mabonga et al., 2019, Siebenmorgen et al., 2020) It also has been limited the recent advance in predicting binding free energy from protein-protein complex structure. (Mobley et al., 2019, Gromiha et al, 2017, Vangone et al., 2015) Therefore, it becomes necessary to acquire more detailed understanding of the intricate nature of molecular interactions at the binding interface that enable us to enhance existing methods and gain microscopic insights on how to effectively modify these PPIs to achieve stronger binding affinity.

One of the most recognized methods to elucidate the individual molecular interactions is alanine-scanning mutagenesis among several experimental and computational studies. (Scott et al., 2016, Rao et al., 2014, Moreira et al., 2007, Nero et al., 2014, Marchand et al., 2022) This method coupled with free energy simulations has demonstrated remarkable success in predicting binding free energy of both small drug molecules (Kortemme et al., 2004, Boukharta et al., 2014) and protein-protein interfaces. (Moreira et al., 2007, Simoes et al., 2017) However, employing alanine scanning for all interfacial residues is time-consuming. Furthermore, site-directed mutagenesis occasionally leads to substantial alterations in protein conformations and undesired perturbations to interactions beyond mutation site, (Dave et al. 2016, Ardejani et al., 2017) which is then difficult to interpret mutation-based analyzed results in order to elucidate how binding affinity arises from underlying molecular interactions.

Binding affinity of protein-protein interactions is not solely determined by the final structure of the complex but also by the changes in free energy during complex formation, which includes environmental changes for interfacial residues. An explicit example of this is the dehydration penalty. For example, the formation of a hydrogen bond at the binding interface may seem favorable for binding affinity, but when considering the dehydration penalty, this is not apparent. Interestingly, interfacial amino acid residues that are involved in hydrogen bonding with surrounding water molecules before

complex formation require the removal of these water molecules during binding, resulting in a free energy cost known as the dehydration penalty. Therefore, when discussing the molecular interactions involved in building up PPIs, it is crucial to consider those influenced by the surrounding water molecules, or solvent-averaged interactions. There remains a challenge to quantitatively isolate magnitude of dehydration penalty for individual interface interaction, though explicit-water free energy simulations naturally account for it.

Here, we present an atomic-level thermodynamics analysis that enables to quantify the contribution of individual interactions to binding free energy, and hence, introduce a new perspective on the nature of molecular interactions that govern the protein-protein binding affinity. (Lee et al., 2022) Our method utilizes a quantity $\Delta f = \Delta E_{\mathrm{u}} + \Delta G_{\mathrm{solv}}$, which comprises the direct interaction energy (ΔE_{u}) between a protein complex and the solvation free energy change (ΔG_{solv}) upon complex formation. (Lazaridis et al., 1999, Lazaridis et al., 2000) This quantity is connected to the binding free energy (ΔG_{bind}) via (Gilson et al., 1997, Chong et al., 2016)

$$\Delta G_{\mathrm{bind}} = \Delta f - T\left(\Delta S_{\mathrm{config}} + \Delta S_{\mathrm{ext}}\right) \qquad (1)$$

, where T represents the temperature, and $\Delta S_{\mathrm{config}}$ and ΔS_{ext} represent the change in configurational and external entropy, respectively. Since protein structures, particularly at the binding interface, usually become more rigid ($-T\Delta S_{\mathrm{config}} > 0$) and experience

a reduction in positional and orientational freedom ($-T\Delta S_{\mathrm{ext}} > 0$) upon complex formation, the driving force for binding is derived from Δf (<0). Hence, it is meaningful to focus on this quantity to quantify the role of individual interactions in binding affinity. The quantity Δf is referred to as the effective binding energy (Gohlke et al., 2004) or solvent-averaged interaction energy (Bryngelson et al., 1995), considering the solvent effect (dehydration penalty) through ΔG_{solv}. Importantly, a formally exact atomic (labeled by a) decomposition, $\Delta f = \sum_a \Delta f_a$, is achievable, allowing for the decomposition of ΔE_{u} using classical force fields and the application of a previously derived decomposition method for ΔG_{solv}. (Chong et al., 2011) This decomposition into individual atomic contributions can be carried out without introducing any mutations, enabling us to analyze the system of interest in its native state. Our method's utility to handle a system of interest is exemplified through its application to SARS-CoV-2 neutralizing antibodies. We provide an illustration that the formation of single contact, such as a hydrogen bond, at the interface has minimal contribution to the binding free energy due to the dehydration penalty. In contrast, the simultaneous formation of multiple atomic contacts favorably impacts the binding affinity. This is attributed to a significant reduction in the dehydration penalty, as the total penalty incurred by multiple contacts is smaller than the sum of individual dehydration penalties of those contacts. By highlighting these findings, we aim to introduce a new perspective on the nature of molecular interactions that govern protein-protein binding affinity.

2.2. Methods

2.2.1. System preparation

We studied three Fab domain antibodies—CV30 (Hurlburt et al., 2020), B38 (Wu et al., 2020), and CB6 (Shi et al., 2020)—targeting the receptor binding domain (RBD) of the SARS-CoV-2 spike protein (Figure 2.1A to Figure 2.1C). Their complex structures were taken from the Protein Data Bank (PDB): the accession codes are 6XE1, 7BZ5, and 7C01 for CV30/RBD, B38/RBD and CB6/RBD, respectively. These antibodies have nearly the same sequences except for the complementarity determining regions (CDRs; see Figure 2.1D).29 While CB6 has a longer heavy-chain CDR (HCDR) 3 than CV30 and B38, the overall Fab structures are quite similar: C_α root mean square deviation to CV30 is 0.24 Å for B38 and 0.33 Å for CB6. The RBD in the respective PDB files has slightly different sequence lengths, and we modified the RBD in B38/RBD and CB6/RBD such that it has the same sequence length (207 residues) as in CV30/RBD. Missing residues were modeled by using the MODELLER program. (Webb et al., 2016) The N- and C-terminals of the RBD were capped by ACE (acetyl) and NME (N-methylamide) groups, respectively. The resulting complex structures were used as inputs to molecular dynamics (MD) simulations. We renumbered the residues in our systems, and the correspondence between our numbering and the one in PDB structures is summarized in Figure 2.2 for CV30/RBD, Figure 2.3 for B38/RBD and Figure 2.4 for CB6/RBD.

Figure 2.1. Fab domain antibodies complexed with the receptor binding domain (RBD) of the SARS-CoV-2 spike protein studied in the present work. (A) CV30/RBD. (B) B38/RBD. (C) CB6/RBD. (D) Sequence alignment of the complementarity determining regions (CDRs).

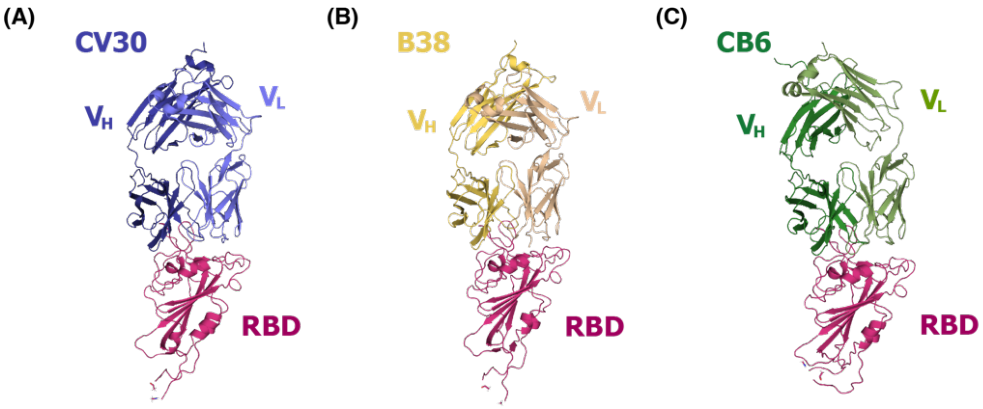

(D)

	HCDR1	HCDR2	HCDR3
CV30	AASGVIVSSNYMS--	VIYSGGSTYYADSVKG---	ARDLDVSGGMDV-----
B38	--SGFIVSSNYMSWV	---SGGSTYYADSVKGRFT	AY------GMDVWGQ--
CB6	AASGFTVSSNYMS--	VIYSGGSTFYADSVKG---	ARVLPMY-G-DYLDY--

	LCDR1	LCDR2	LCDR3
CV30	RASQSVSSSYLAW	GASSRATG	--QQYGSS-PQT-
B38	RASQGISS-YLAW	AASTLQSG	--QQLNSYPPYT-
CB6	RASQSISR-YLNW	AASSLQSG	YCQQSYSTPPE--

Figure 2.2. Correspondence between the numbering of amino acid residues used in the present work and the one in the PDB structure (6XE1) for CV30/RBD.

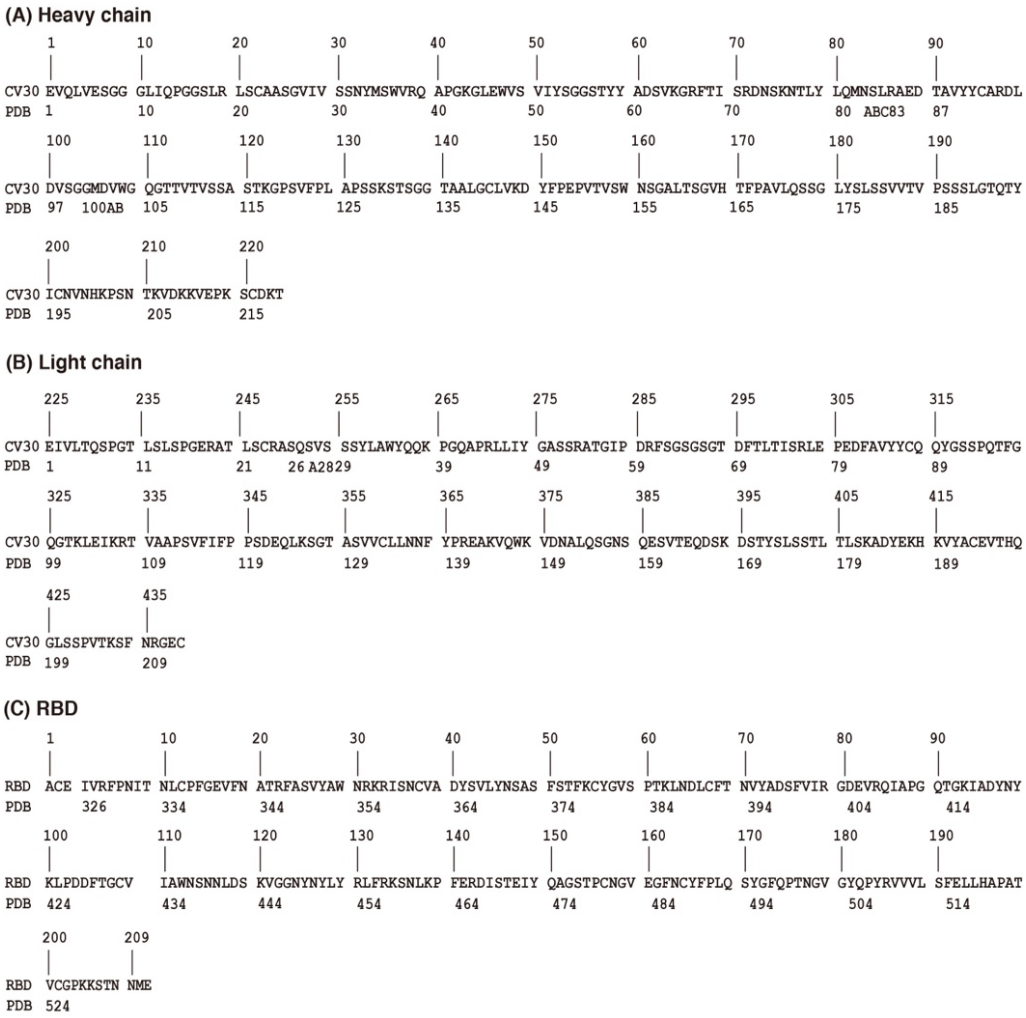

Figure 2.3. Correspondence between the numbering of amino acid residues used in the present work and the one in the PDB structure (7BZ5) for B38/RBD.

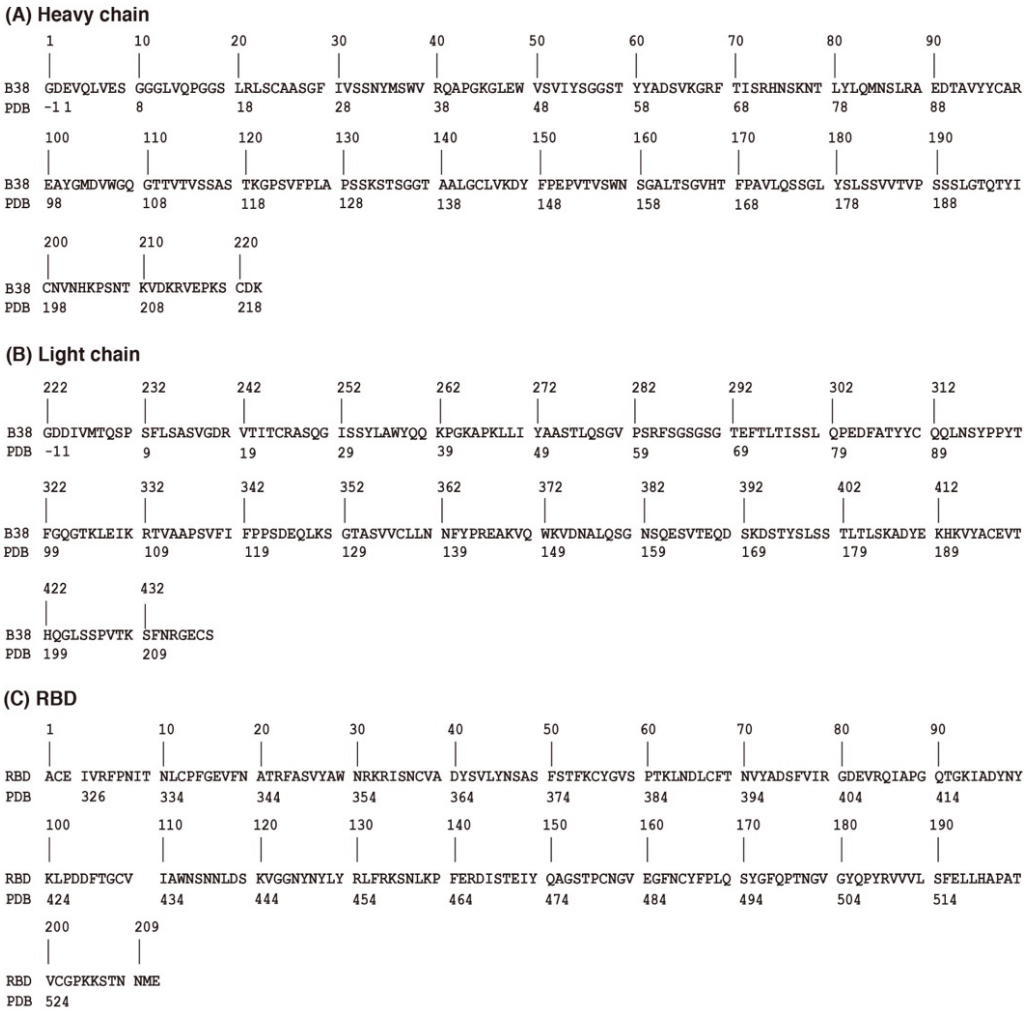

Figure 2.4. Correspondence between the numbering of amino acid residues used in the present work and the one in the PDB structure (7C01) for CB6/RBD.

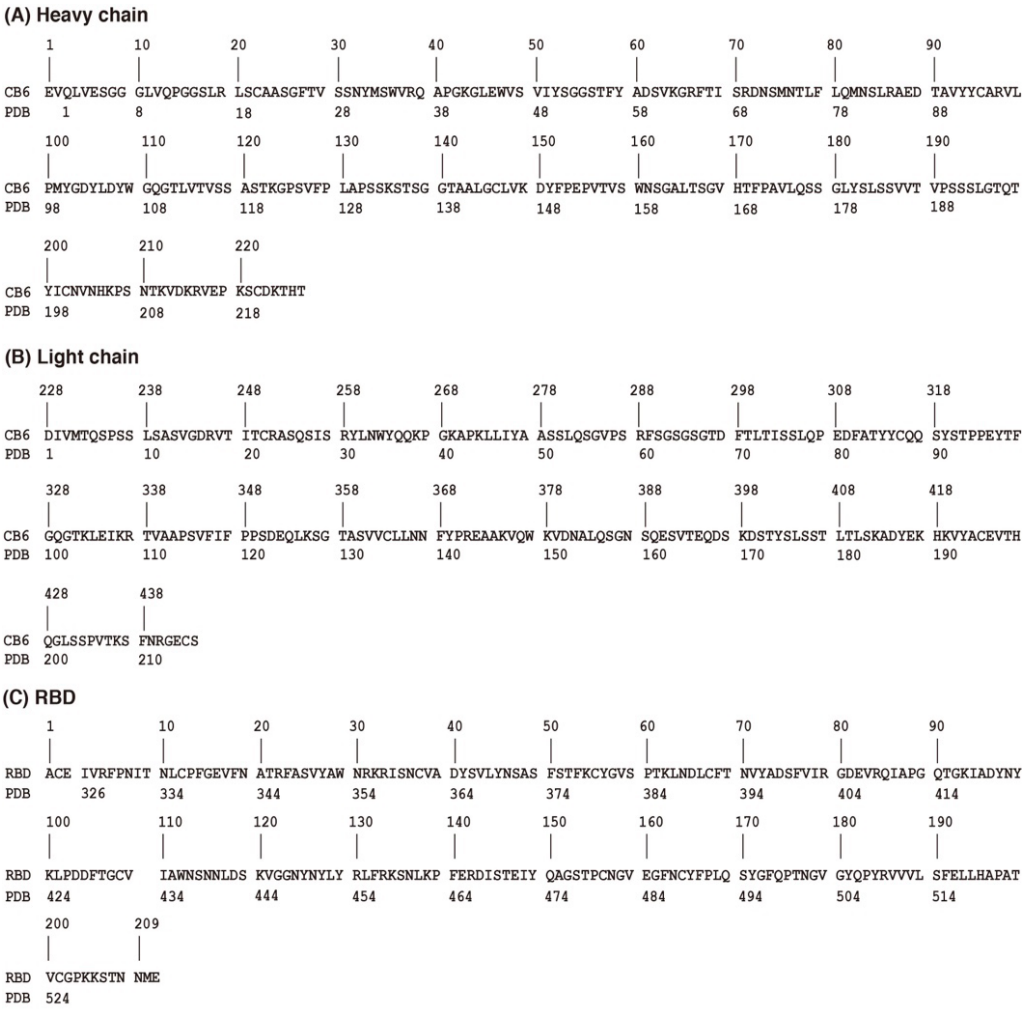

2.2.2. MD simulations

The AMBER20 package (Case et al., 2020) was utilized to perform MD simulations. AMBER ff14SB (Maier et al., 2015) was employed for proteins and ions, and the systems were solvated by TIP3P waters. (Jorgensen et al., 1983) Besides neutralizing counter ions, additional Na^+ and Cl^- ions were added to reach 150 mM ionic strength. Prior to simulations, 500 steps of the steepest descent minimization were performed followed by 500 steps of conjugate gradient minimization with 500 kcal/(mol · Å^2) harmonic restraints on protein heavy atoms. Additionally, 1000 and 1500 steps of the steepest descent and conjugate gradient minimization without harmonic restraints were carried out. The systems were heated up with 20 ps NVT simulation with 10 kcal/(mol · Å^2) restraints, followed by 200 ps NPT equilibration simulation at 300 K and 1 bar without restraints. Finally, 100 ns NPT production runs were conducted three times for each system. The temperature and pressure were kept to 300 K and 1 bar by Langevin thermostat (Pastor et al., 1988) and Berendsen barostat. (Berendsen et al., 1984) 10 Å cutoff was used for short-range interactions, and long-range electrostatic forces were handled by the Particle Mesh Ewald method. (Darden et al., 1993)

2.2.3. Effective binding energy calculation

We extracted complex structures every 1 ns, resulting in 300 MD snapshots from the three independent simulations of 100 ns length. All ions and water molecules were removed in yielding the snapshots.

These simulated complex structures were used for computing the effective binding energy Δf,

$$\Delta f = \Delta E_{\mathrm{u}} + \Delta G_{\mathrm{solv}} \qquad (2)$$

Here, E_u is the (gas-phase) interaction potential, G_{solv} is the solvation free energy, and ΔX refers to the change upon complex formation:

$$\Delta X = X_{\mathrm{complex}} - (X_{\mathrm{antibody}} + X_{\mathrm{RBD}}) \quad (3)$$

In the present work, both antibody and RBD structures were taken from the simulated complex structures (referred to as the one-trajectory approach). In this case, ΔE_{u} is given by the direct interaction energy between antibody and RBD comprising the Lennard-Jones (LJ) and electrostatic terms:

$$\Delta E_{\mathrm{u}} = \sum_{\mathrm{a,b}} \left[u_{\mathrm{ab}}^{(\mathrm{LJ})} + u_{\mathrm{ab}}^{(\mathrm{elec})} \right] \qquad (4)$$

in which a and b label constituent atoms. The atomic decomposition of ΔE_{u} can hence be easily be obtained:

$$\Delta E_{\mathrm{u}} = \sum_{a} \Delta E_{\mathrm{u,a}}; \quad \Delta E_{\mathrm{u,a}} = \sum_{\mathrm{b}} \left[u_{\mathrm{ab}}^{(\mathrm{LJ})} + u_{\mathrm{ab}}^{(\mathrm{elec})} \right] \qquad (5)$$

The solvation free energy G_{solv} in this work was calculated by employing the three-dimensional reference interaction site model (3D-RISM) theory with the Kovalenko-Hirata closure, (Imai et al., 2006, Kovalenko et al., 2003) which allows us to compute G_{solv} for a given protein structure. ΔG_{solv} can be obtained by applying the 3D-RISM theory individually to the complex, antibody and RBD

structures and then using Equation 3, and this was repeated for 100 structures taken from each simulation trajectory with a 1 ns time interval; average and standard error were then estimated based on the three independent trajectories. We used our in-house program in solving the 3D-RISM equations on a grid of 256 × 256 × 256 points with a spacial resolution of 0.625 Å along each direction. A formally exact decomposition method of ΔG_{solv} has been derived (Chong et al., 2011), with which we have

$$\Delta G_{\mathrm{solv}} = \sum_{\mathrm{a}} \Delta G_{\mathrm{solv,a}}\,; \quad \Delta G_{\mathrm{solv,a}} = \Delta G_{\mathrm{solv,a}}^{(\mathrm{LJ})} + \Delta G_{\mathrm{solv,a}}^{(\mathrm{elec})} \qquad (6)$$

The atomic decomposition of the effective binding energy, $\Delta f = \sum_a f_a$, follows from Equations 2, 5 and 6. This is the basis of our atomic-level thermodynamics analysis. In the following, results will be reported in the form of the residue-wise decomposition, $\Delta f = \sum_i f_i$, by summing up atomic contributions in residue i, $\Delta f_i = \sum_{a \in i} \Delta f_a$.

2.3. Results and discussion

2.3.1. Overall trends in effective binding energy

We investigated three Fab domain antibodies—CV30, B38 and CB6—forming a complex with the receptor binding domain (RBD) of the SARS-CoV-2 spike protein (Figure 2.1). Molecular dynamics simulations were conducted for CV30/RBD, B38/RBD and CB6/RBD complex systems for their structural and thermodynamics analyses. Three independent production runs of 100 ns length were carried out from which averages and standard errors were estimated. The complex structures were stable during the simulations (Cα root

mean square deviations from the respective PDB structures are 3.4 ± 0.5, 3.3 ± 0.6 and 2.4 ± 0.2 for CV30/RBD, B38/RBD and CB6/RBD, respectively). We computed the effective binding energy $\Delta f = \Delta E_{\mathrm{u}} + \Delta G_{\mathrm{solv}}$ based on these simulated complex structures.

We find that CB6/RBD ($\Delta f = -31.4 \pm 1.7$ kcal/mol) exhibits the strongest binding in terms of Δf, followed by CV30/RBD ($\Delta f = -30.0 \pm 1.4$ kcal/mol) and B38/RBD ($\Delta f = -28.2 \pm 1.0$ kcal/mol). This trend is in accord with the experimental observations: CB6 shows the strongest binding affinity (K_{D}= 2.5 nM and IC_{50} = 0.036 μg/mL), followed by CV30 (K_{D} = 3.6 nM and IC_{50} = 0.03 μg/mL) and B38 (K_{D} = 70.1 nM and IC_{50} = 0.177 μg/mL). (Hurlburt et al., 2020) To elucidate how such binding affinity is determined from underlying molecular interactions, we decomposed Δf into contributions Δf_i from individual residues (labeled i), $\Delta f = \sum_i f_i$. Since all the component proteins under study have nonzero net charges (see Figure 2.1; all of CV30, B38, CB6 and RBD are positively charged), we first partitioned Δf into contributions from neutral and charged residues (**Table 2.1** and Figure 2.5). It is clearly seen that favorable (negative) contributions to Δf are dominantly provided by neutral residues. The overall unfavorable (positive) contributions to Δf from charged residues are understandable from the fact that all the antibodies and RBD are positively charged, i.e., the net electrostatic interaction between the antibody and RBD should be repulsive.

Table 2.1. Effective binding energy Δf and neutral- and charged-residue contributions

	Δf (kcal/mol)	neutral residues	charged residues
CV30/RBD	-30.0 ± 1.4	-31.2 ± 0.3	1.2 ± 1.3
B38/RBD	-28.2 ± 1.0	-33.4 ± 0.7	5.2 ± 0.4
CB6/RBD	-31.4 ± 1.7	-33.3 ± 1.5	1.9 ± 1.2

Figure 2.5. Contributions to the effective binding energy Δf (in kcal/mol) from neutral (cyan bars) and charged (orange bars) residues.

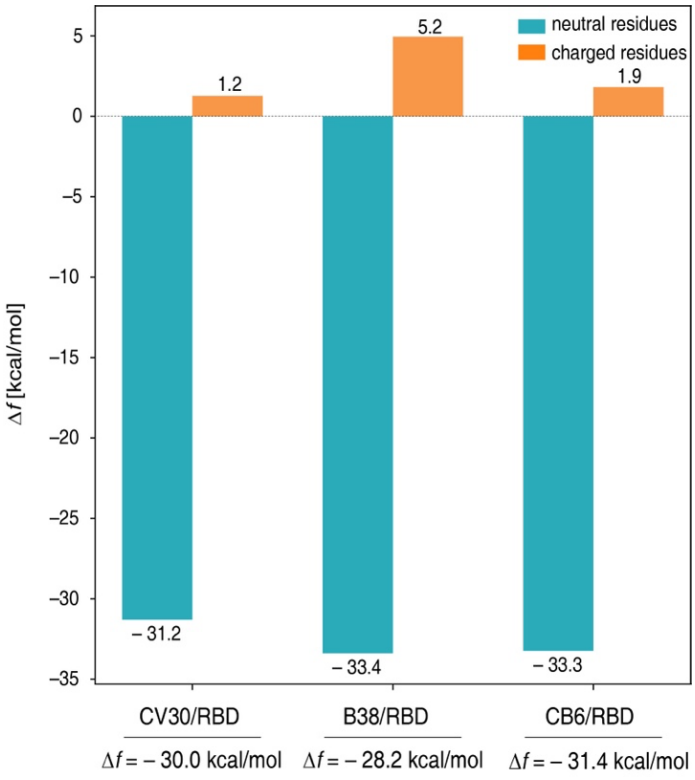

2.3.2. Connection between effective binding energy and molecular interactions

We next analyze how the magnitude of individual Δf_i is connected to underlying molecular interactions. For this purpose, we show in Figure 2.6A the residue-wise decomposition Δf_i and in Figure 2.6B the heavy-atom contact map for CV30/RBD (a heavy atom contact is considered formed if the heavy atom distance is <4.5 Å). Corresponding results for B38/RBD and CB6/RBD are presented in Figure 2.7 and Figure 2.8, respectively. In the following, we will mainly refer to Figure 2.6 to succinctly describe our results.

We first notice that nonzero Δf_i values originate mostly from the complementarity determining regions (CDRs) in the antibody and from those residues in RBD making contacts with CDRs (shaded blue in Figure 2.6A). This is natural because it is the CDRs in the antibody that specifically interact with the target (RBD). We shall be particularly interested in those residues whose Δf_i values are more negative than -1 kcal/mol. Since the magnitude of such Δf_i values is much stronger than the thermal energy ($k_{\mathrm{B}}T \sim 0.6$ kcal/mol), those residues can be considered significant contributors to binding affinity. Significant residues in this sense are listed in **Table 2.2** (those of B38/RBD and CB6/RBD complex are listed in **Table 2.3** and **2.4**, respectively). The dominance of neutral residue contributions mentioned above is apparent from the fact only a few charged residues from each system show up in this table. Significant residues are also marked by the dots along the horizontal (residues in CV30) and vertical (residues in RBD) axis labels in Figure 2.6B. We observe from a comparison of Figure 2.6A and Figure 2.6B that

the mere presence of contacts for a given residue does not warrant its thermodynamic significance. This implies that the contact map alone is insufficient for discriminating significant and insignificant residues, and more detailed analysis on the nature of interface interactions is necessary.

In this regard, we notice that molecular interactions at the binding interface can be broadly classified into hydrogen bonds (interaction between N/O atoms mediated by a hydrogen atom; considered formed if the N/O distance is <3.5 Å; salt-bridges are also counted as hydrogen bonds) and hydrophobic carbon-carbon (CC) contacts (considered formed if the CC distance is <4.5 Å). The average numbers of these atom-atom contacts during the simulations are added in **Table 2.2, 2.3, and 2.4** for CV30/RBD, B38/RBD, and CB6/RBD complex, respectively. We find that the presence of simultaneous multiple contacts is the characteristic of this table listing thermodynamically significant residues: not only the average number of hydrogen bonds and CC contacts typically exceeds 1, but also in most cases both of hydrogen bonds and CC-bonds are simultaneously present. This situation is illustrated in Figure 2.6C in which hydrogen bonds are denoted by the dashed lines and carbon atoms represented by spheres; the presence of CC contacts can be inferred from that of neighboring spheres. For example, the side chain of S56 in CV30 (Δf_i = −2.4 kcal/mol) forms more than one hydrogen bonds and CC contacts simultaneously with the surrounding residues; in L131 of RBD (Δf_i = −1.7 kcal/mol), less than one hydrogen bond is present on average, but several CC contacts are formed simultaneously; and the side chain of K93 in RBD (Δf_i = −2.8 kcal/mol) forms about two hydrogen bonds simultaneously and its

hydrophobic neck makes a large number of CC contacts (see **Table 2.2**). Furthermore, a simple regression analysis of Δf_i in terms of hydrogen bonds and CC contacts, presented in Figure 2.9, indicates that hydrogen bonds provide larger contributions to Δf_i than CC contacts, and this roughly explains the difference in Δf_i values shown in Figure 2.6C. Thus, the simultaneous presence of multiple interactions is the genuine characteristic of those residues that significantly contribute to binding affinity.

Figure 2.6. (A) Residue-decomposed Δf_i versus residue number for CV30/RBD. Black, red, and blue bars refer to neutral, negatively charged and positively charged residues, respectively. Heavy- and light-chain complementarity-determining regions (HCDRs and LCDRs) in the antibody and the residues in RBD that contact with these regions are shaded blue. (B) Heavy-atom contact map. Only those contacts whose average populations is >10% during the simulations are included. The dots along the horizontal (antibody) and vertical (RBD) axes mark those residues whose Δf_i values are <-1.0 kcal/mol. (C) Illustration of representative interfacial contacts. Residues in RBD are marked with the asterisk.

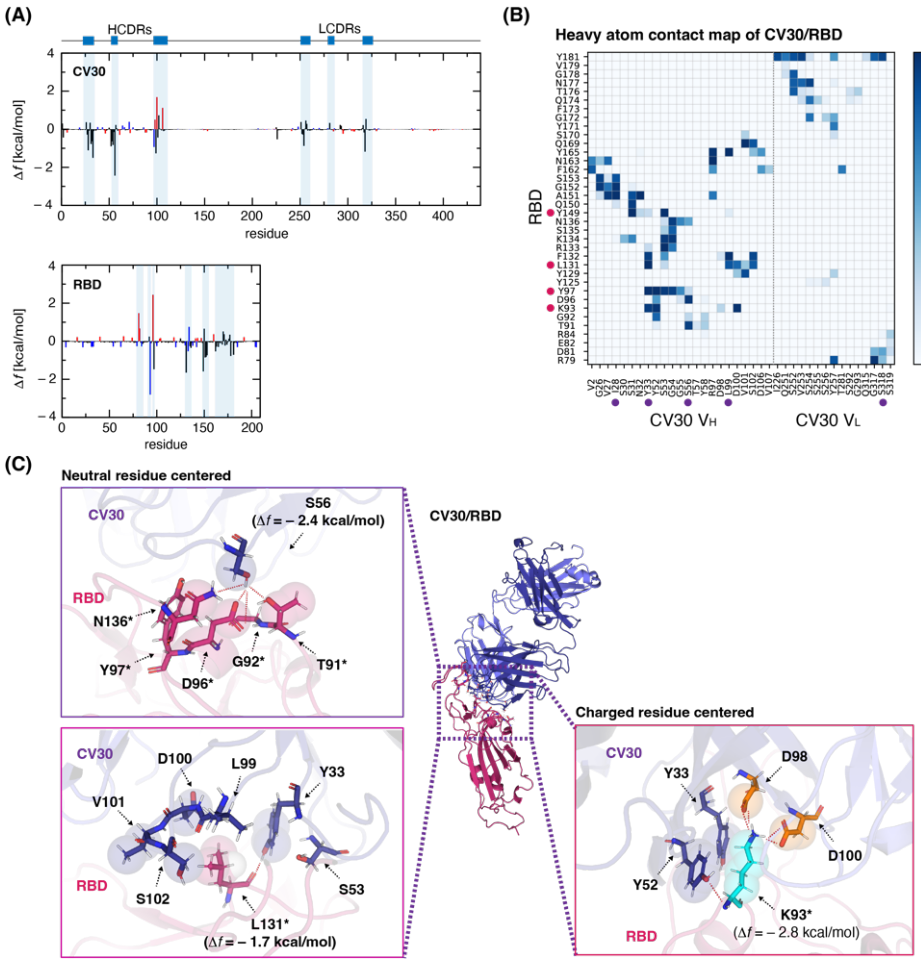

Figure 2.7. (A) Residue-decomposed Δf_i versus residue number for B38/RBD. Black, red, and blue bars refer to neutral, negatively charged and positively charged residues, respectively. Heavy- and light-chain complementarity-determining regions (HCDRs and LCDRs) in the antibody and the residues in RBD that contact with these regions are shaded blue. (B) Heavy-atom contact map. Only those contacts whose average populations is >10% during the simulations are included. The dots along the horizontal (antibody) and vertical (RBD) axes mark those residues whose Δf_i values are <-1.0 kcal/mol. (C) Illustration of representative interfacial contacts. Residues in RBD are marked with the asterisk.

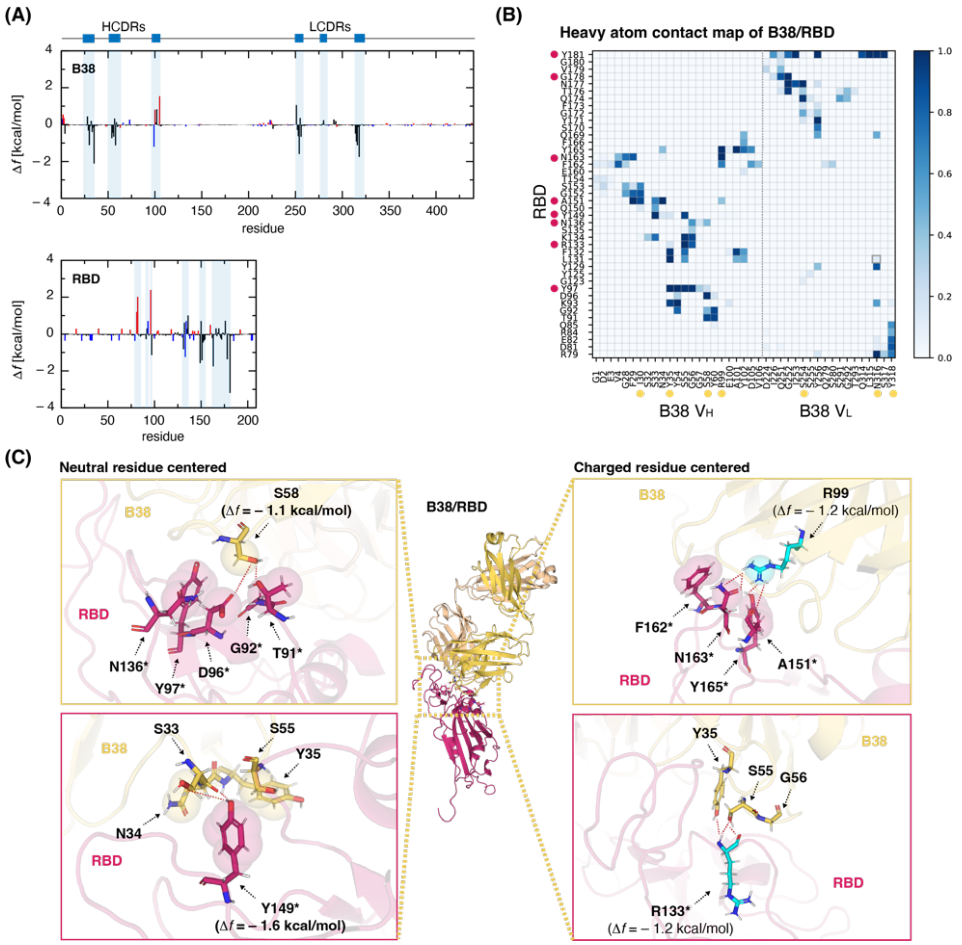

Figure 2.8. (A) Residue-decomposed Δf_i versus residue number for CB6/RBD. Black, red, and blue bars refer to neutral, negatively charged and positively charged residues, respectively. Heavy- and light-chain complementarity-determining regions (HCDRs and LCDRs) in the antibody and the residues in RBD that contact with these regions are shaded blue. (B) Heavy-atom contact map. Only those contacts whose average populations is >10% during the simulations are included. The dots along the horizontal (antibody) and vertical (RBD) axes mark those residues whose Δf_i values are <-1.0 kcal/mol. (C) Illustration of representative interfacial contacts. Residues in RBD are marked with the asterisk.

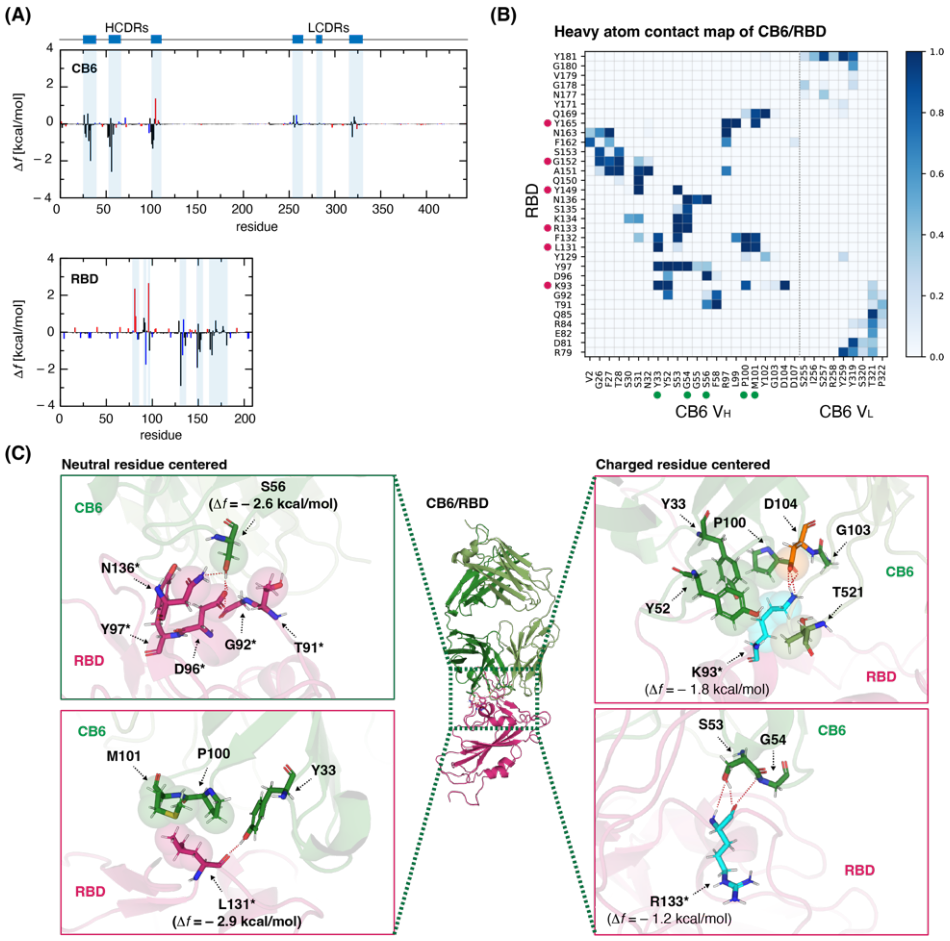

Figure 2.9. Linear regression analysis of the residue-decomposed effective binding energy (Δf_i) for neutral residues in terms of the number of hydrogen bonds ($\omega_1 x_{\mathrm{HB}}$), the number of CC contacts ($\omega_2 x_{\mathrm{CC}}$), and the solvent accessible surface area (SASA) of the side-chain polar atoms ($\omega_3 x_{\mathrm{SASA}}$), $\Delta f_i = \omega_1 x_{\mathrm{HB}} + \omega_2 x_{\mathrm{CC}} + \omega_3 x_{\mathrm{SASA}} + b$. The weights ($\omega$' s) and intercept ($b$) determined from the linear regression analysis are $\omega_1 = -0.72$, $\omega_2 = -0.14$, $\omega_3 = -0.03$ and $b = -0.03$, indicating that the number of hydrogen bonds ($\omega_1 = -0.72$) more significantly impacts Δf_i than that of CC contacts ($\omega_2 = -0.14$).

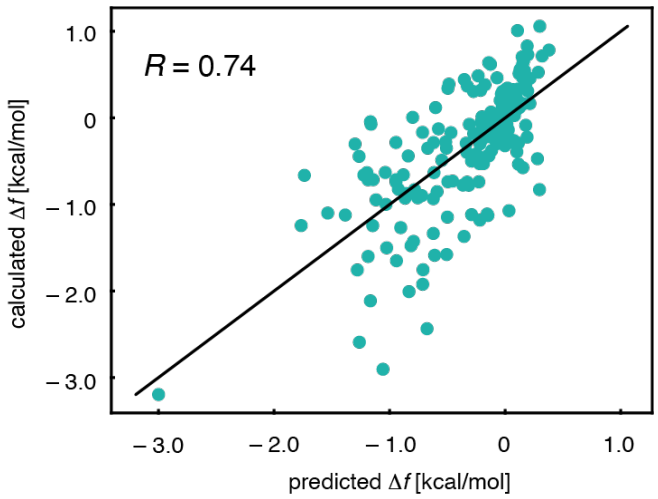

Table 2.2. Residue-wise effective binding energy Δf_i versus the interface contacts in CV30/RBD complex

residue[a]	Δf_i (kcal/mol)	# of hydrogen bonds[b]	# of CC contacts[c]
CV30/RBD complex			
I28	−1.1	0.6	0.6
S318	−1.2	0.7	1.6
L99	−1.3	0.0	8.5
Y97*	−1.5	1.4	4.1
Y33	−1.5	1.0	9.7
Y149*	−1.6	1.3	2.1
L131*	−1.7	0.8	4.6
S56	−2.4	1.6	1.5
K93*	−2.8	1.8	9.5

Note: [a] Residues from RBD are marked by the asterisk. [b] Average number of hydrogen bonds formed with the surrounding residues. [c] Average number of carbon-carbon (CC) contacts formed with the surrounding residues.

Table 2.3. Residue-wise effective binding energy Δf_i versus the interface contacts in B38/RBD complex

residue[a]	Δf_i (kcal/mol)	# of hydrogen bonds[b]	# of CC contacts[c]
B38/RBD complex			
I30	−1.1	0.8	0.3
N316	−1.1	3.6	0.5
S58	−1.1	1.2	0.8
T97*	−1.1	1.4	2.6
R99	−1.2	3.2	1.2
R133*	−1.2	2.7	0.0
G178*	−1.4	1.1	0.0
A151*	−1.4	1.9	1.1
Y149*	−1.6	1.1	2.1
S254	−1.6	2.3	2.3
Y318	−1.8	1.4	5.7
N163*	−1.8	2.5	1.2
Y35	−2.1	1.3	8.6
Y181*	−3.2	2.5	17.4

Note: [a] Residues from RBD are marked by the asterisk. [b] Average number of hydrogen bonds formed with the surrounding residues. [c] Average number of carbon-carbon (CC) contacts formed with the surrounding residues.

Table 2.4. Residue-wise effective binding energy Δf_i versus the interface contacts in CB6/RBD complex

residue[a]	Δf_i (kcal/mol)	# of hydrogen bonds[b]	# of CC contacts[c]
CB6/RBD complex			
G152*	−1.1	0.4	0.0
P100	−1.1	0.3	11.1
Y165*	−1.2	1.1	9.2
G54	−1.2	2.3	0.0
R133*	−1.2	2.6	0.0
M101	−1.3	0.0	7.2
K93*	−1.8	2.2	6.1
Y149*	−1.9	1.2	2.0
Y33	−2.0	1.0	5.9
S56	−2.6	2.4	1,7
L131*	−2,9	1.0	5.0

Note: [a] Residues from RBD are marked by the asterisk. [b] Average number of hydrogen bonds formed with the surrounding residues. [c] Average number of carbon-carbon (CC) contacts formed with the surrounding residues.

2.3.4. Why simultaneous multiple interactions are thermodynamically crucial

In order to understand why such interactions are crucial, let us analyze Δf_i from a different viewpoint. In general, the direct interaction energy ($\Delta E_{\mathrm{u},i}$) and the solvation free energy change ($\Delta G_{\mathrm{solv},i}$) exhibits an anti-correlation. This is because, e.g., the formation of a contact between two interface residues ($\Delta E_{\mathrm{u},i} < 0$) necessarily involves the dehydration of those residues ($\Delta G_{\mathrm{solv},i} > 0$). In fact, if we examine the correlation between $\Delta E_{\mathrm{u},i}$ and $\Delta G_{\mathrm{solv},i}$ taken from all the three antibody/RBD systems, we obtain almost a perfect negative correlation (Figure 2.10A; Pearson's correlation coefficient is -0.997). Thus, $\Delta f_i = \Delta E_{\mathrm{u},i} + \Delta G_{\mathrm{solv},i} \approx 0$ is expected on general ground, and this is indeed the case as demonstrated in Figure 2.10B showing a delta-function like distribution of Δf_i peaked around 0. This holds even when a hydrogen bond is involved as exemplified in Figure 2.10C: a large gain in the direct interaction energy ($\Delta E_{\mathrm{u},i} = -4.9$ kcal/mol for G317 and -10.2 kcal/mol for R79) upon a hydrogen bond formation between G317 of CV30 and R79 of RBD is almost perfectly canceled by the dehydration penalty ($\Delta G_{\mathrm{solv},i} = +4.7$ and $+10.0$ kcal/mol, respectively), resulting in $\Delta f_{\mathrm{i}} \approx 0$ ($\Delta f_i = -0.2$ and -0.3 kcal/mol).

This situation is altered when multiple interactions are present at the same time. This is because there are common water molecules hydrating those atoms that are to form multiple contacts upon complex formation. Thus, the total dehydration penalty for multiple contacts is smaller than a sum of what would be expected for individual dehydrations of those contacts, i.e., the dehydration penalty is

significantly alleviated for multiple contacts. This is demonstrated in Figure 2.11 showing individual residues' Δf_i (green circles), $\Delta E_{\mathrm{u},i}$ (cyan circles), and $\Delta G_{\mathrm{solv},i}$ (orange circles) versus the number of hydrogen bonds taken from all the antibody/RBD systems. Up to the number of hydrogen bonds ≈ 1, $\Delta E_{\mathrm{u},i}$ and $\Delta G_{\mathrm{solv},i}$ nearly cancel each other, and Δf_i remains close to 0. However, when multiple hydrogen bonds are present (the number of hydrogen bonds > 1), the energetic gain (decrease in $\Delta E_{\mathrm{u},i}$) is larger than the dehydration penalty (increase in $\Delta G_{\mathrm{solv},i}$). This leads to Δf_i of favorable (negative) values for multiple interactions.

Dehydration penalty is involved in any biological organization processes—folding, binding, and coupled folding and binding—that occur in aqueous environments. One possible way to alleviate such an inevitable hindrance is through the simultaneous formation of multiple interactions discussed here. Indeed, it has been shown that those residues that participate in the secondary structure (hydrogen bonds) and in the hydrophobic core (CC contacts) at the same time are the ones that most stabilize the protein folded structure. (Cho et al., 2021) The simultaneous formation of multiple contacts has also been demonstrated to be the distinguishing characteristic unique to protein folding transition path. (Chong et al., 2021) Intrinsically disordered proteins do not possess well-defined secondary structures when isolated, but they do so upon binding with a partner protein. Thermodynamically, this is because enough stabilizing energy cannot be gained just by forming secondary structures (intramolecular hydrogen bonds) due to the dehydration penalty; (Dill et al., 1990) but additional side-chain interactions with the partner protein brings about the secondary structure formation since the dehydration penalty

gets weakened. (Chong et al., 2019, Chong et al., 2019) Such a perspective, gained through the application of atomic-level thermodynamics analysis, will be useful also in developing protein therapeutics of improved binding affinity.

Figure 2.10. (A) Scatter plot of $\Delta E_{\mathrm{u},i}$ versus $\Delta G_{\mathrm{solv},i}$ taken from all the antibody/RBD systems. (B) Histogram of Δf_i values taken from all the antibody/RBD systems. (C) Illustration of how the gain in the direct interaction energy ($\Delta E_{\mathrm{u},i}$) upon the formation of a hydrogen bond at the binding interface is nearly canceled by the dehydration penalty ($\Delta G_{\mathrm{solv},i}$).

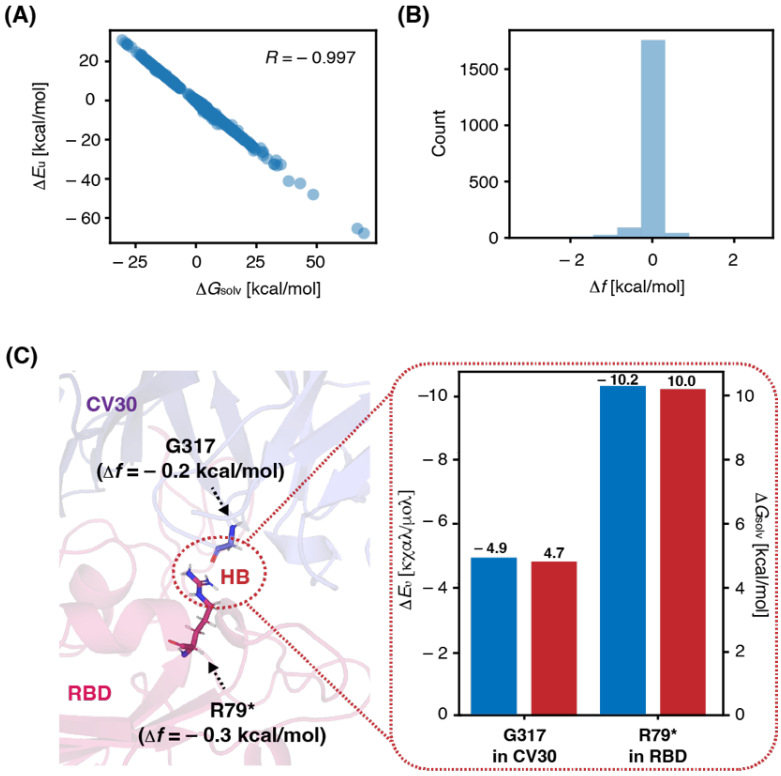

Figure 2.11. Individual residues' Δf_i (green circles), $\Delta E_{\mathrm{u},i}$ (cyan circles), and $\Delta G_{\mathrm{solv},i}$ (orange circles) for neutral residues versus the number of hydrogen bonds taken from all the antibody/RBD systems. Solid curves are based on the linear fits to the respective data points, and the resulting slopes are indicated in the figure. Red dashed curve denotes the location of 0 kcal/mol.

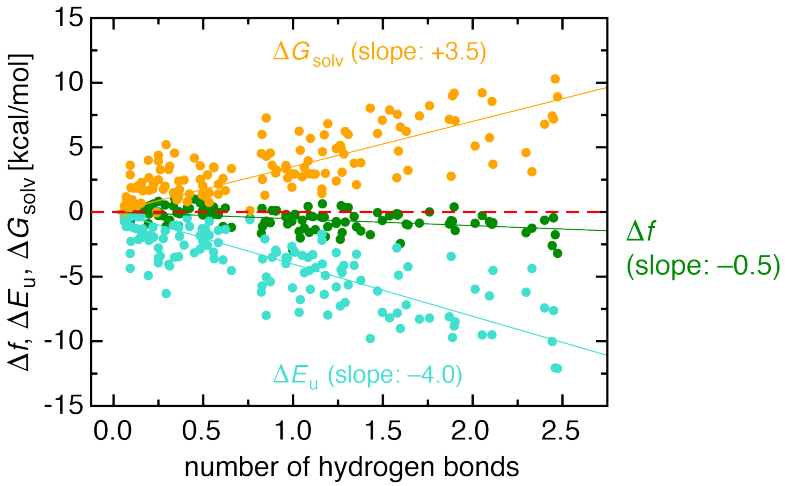

2.4. Conclusions

In this work, we present an atomic-level thermodynamics analysis that quantifies how individual amino acids at the binding interface favorably contribute to protein–protein binding free energy. Distinguishing characteristics of our analysis method is that it does not require introducing any mutations as in the alanine-scanning method and that the solvent effect— dehydration penalty—is properly taken into account via solvation free energy. The utility of our analysis method is illustrated through its application to SARS-CoV-2 neutralizing antibodies. We find that a single contact such as a hydrogen bond at the binding interface barely contributes to the binding free energy: a favorable direct interaction energy gained by the contact formation is nearly canceled by the dehydration penalty. On the other hand, the formation of simultaneous multiple contacts is demonstrated to significantly contribute to binding affinity. This is because the total dehydration penalty for multiple contacts is smaller than a sum of penalties expected for individual dehydrations of single contacts. We believe that our results provide a new perspective for rationalizing protein–protein interactions and designing protein therapeutics of improved binding affinity.

3. Substrate Selectivity in Human and Pseudomonas Kynureninases: Mechanistic Insight from Molecular Dynamics Simulations

3.1. Introduction

Enzyme engineering has been in a rapid progress in potent drug development as a special class of protein-based therapeutics. Enzymes have the potential to be applied in a wide range of disease such as cancer, heart attacks, and genetic disorders by catalyzing relevant chemical reactions by specifically interacting with target. (Dimitrov, 2012, Vellard, 2017) Among widely used enzyme engineering strategies, improving the specific activity is one of the important studies in enzyme therapeutics. Viewed from the perspective of rational design, it should be accompanied by the detailed knowledge of enzyme structure, function as well as mechanism. (Chen, 2001)

With the availability of structural and coevolutionary information, there has been an unprecedented development in computational approaches to make enzymes with desired properties. (Li et al., 2012, Welborn et al., 2019) Moreover, recently emerging machine learning approach has become popular since it can generate structures for unseen enzyme mutants and predict the catalytic properties with its advantage of generalizability. (Mazurenko et al., 2020, Feehan et al., 2021) Compared to the state-of-art approaches, however, Molecular Dynamics (MD) simulations is a useful tool to ascertain the catalytic mechanism of enzymes occurring in cellular

compositions by calculating quantitative data of thermodynamics and kinetics properties. (Kiss et al., 2010, Garcìa-Guevara et al., 2015) For example, Grottesi and co-workers revealed the characteristic residues in enzyme active site which modulate drug behaviors and interdomain interactions stabilizing the active state of catalytic pocket by investigating the conformational dynamics of SARS-CoV-2 chymotrypsin-like protease (3CLpro) via all-atom MD simulations. (Grottesi et al., 2020) In addition, Bunzel and co-workers showed the relation between activation of heat capacity and protein dynamics by conducting MD simulations and statistical thermodynamics analysis. They gave evidence that packed solvent-exposed loops to the active site across evolution leads to better stabilized transition-state, which includes the negative activation of heat capacity. (Bunzel et al., 2021) Such precedent works provide important opportunities for investigating molecular mechanism via MD simulations coupled with statistical studies, and therefore facilitate the creation of new enzyme.

In this chapter, we present computational studies aimed at exploring the substrate selectivity differences between human kynureninase (HsKYNU) and pseudomonas kynureninase (PfKYNU) against the two substrates 3-hydroxylated kynurenine (3-OH-KYN) and L-kynurenine (KYN). Through explicit-water MD simulations, we investigated the distinct binding kinetics that contribute to the superior K_D values exhibited by PfKYNU for both substrates. Additionally, we observed the predominant binding conformations associated with enhanced catalytic efficiency. To further elucidate the key interactions governing the bound and unbound states of enzyme-substrate complexes, we performed residence time analysis using 50 replicated MD trajectories. Thereby, we aim to uncover the binding

characteristics underlying the divergent substrate selectivity and provide insights into the distinct kinetics observed in HsKYNU and PfKYNU.

3.2. Methods

3.2.1. System preparation

All calculations were conducted using the X-ray structures of human Kynureninase (HsKYNU; PDB code 3E9K) and pseudomonas Kynureninase (PfKYNU; PDB code 1QZ9). The missing residues in the original PDB files were modeled by using MODELLER software. (Webb, et al., 2016) To obtain the symmetric protein conformation, the PyMoL plugin was utilized. Molecular docking of 3-hydroxylated kynurenine (referred to as 3-OH-KYN) and L-kynurenine (referred to as KYN) were conducted using GalaxyDock3 (Yang et al., 2019). For docking, the substrate binding site was assigned based on the inhibitor site and the PEG site in the original X-ray structure of HsKYNU and PfKYNU, respectively. The final enzyme-substrate complex structure to be used for initial structure for MD simulation was selected based on two criteria: (1) the distance between amine group of substrates and C4A of PLP is within 3.5 Å, and (2) it has the lowest docking score. This selection is crucial as the enzyme reaction initiates with the transamination between the amine group of substrate and the internal aldimine linkage of PLP (C4A) and LYS247 (amine).

3.2.2. Molecular Dynamics simulations

All-atom molecular dynamics (MD) simulations were carried out using PMEMD-cuda module of AMBER 20 package (Case et al., 2020), employing the ff14SB force field. (Maier et al., 2015) Each of four enzyme-substrate combinations, HsKYNU/3-OH-KYN,

HSKYNU/KYN, PfKYNU/3-OH-KYN, PfKYNU/KYN, was solvated in a cubic box using TIP3P water molecules. (Jorgensen et al., 1983) Counter ions were added to achieve the neutral pH and the concentration of 150 mM NaCl. The system underwent energy minimization, including 500 steps of steepest descent minimization followed by 500 steps of conjugate gradient minimization. This was followed by the second energy minimization, consisting of 1,000 steps of steepest descent minimization followed by 1,500 steps of conjugate gradient minimization. The equilibration process involved three steps in two phases. In the first equilibration step, the system was heated from 0K to 310 K over 100 ps with weak harmonic restraints of 10.0 kcal/(mol·Å^2) applied to entire simulation system in the NVT ensemble. The second equilibration step applied the same amount of harmonic restraints to the backbone atoms of the enzyme-substrate complexes for 100 ps. In the third equilibration step, 1.0 kcal/(mol·Å^2) of harmonic restraints were applied to Cα atoms of the complex system for 100 ps. The final equilibration phase was performed in the NPT ensemble by Langevin thermostat (Pastor et al., 1988) and Berendsen barostat (Berendsen et al., 1984) for 4 ns without restraints. Subsequently, production simulation was conducted for 200 ns, which was repeated 10 times for each system. Additional production simulation was performed for 100 ns, which was 50 times for each system, in order to gather more informative data from MD trajectories. The choice of 100 ns was made based on the observation that substrates typically exited the binding pocket before this time, indicating an unbound state if they did not return to the binding pocket. For handling short-range interactions, a 10 Å cutoff was employed. On the other hand, long-range electrostatic

forces were handled by the Particle Mesh Ewald method. (Darden et al., 1993)

3.2.3. Trajectory Analysis

The MD trajectories were analyzed using a combination of CPPTRAJ (Roe et al., 2013) and our own Python script. Hydrogen bonds were identified when distance between the atoms X and Y in hydrogen bonds X-H···Y was within 3.5 Å, where X and Y represents nitrogen (N) and oxygen (O) atom. To access the presence of substrates in the binding pocket during the simulations, VMD software was employed.

3.3. Results and Discussion

3.3.1. Hydrogen bond analysis of the human and pseudomonas kynureninase complexes

We first compared structural dynamics of HsKYNU and PfKYNU by Cα RMSD calculation. Except the modeled regions, the RMSD values remained stable without substantial fluctuations, below 4 Å. Therefore, we focused on regions around the active site. Throughout the MD simulations, we observed distinct binding conformations of both substrates (3-OH-KYN and KYN) depending on the enzyme (HsKYNU or PfKYNU) they complex with. In some cases, the substrates even detached from the binding pocket in short time. To gain deeper insights into these dynamics, we looked into molecular details by examining hydrogen bond populations formed between substrates and surrounding residues throughout the simulations. Specifically, we captured hydrogen bonds in each symmetry-related monomer (the active site is located in the homo-dimeric interface of the enzyme) when the distance between N and O atoms is within 3.5 Å in the MD snapshots. We calculated the hydrogen bond populations for both complexes over the course of the 200 ns simulations, and only those with populations exceeding 10 % are shown in **Table 3.1** and **Table 3.2** for HsKYNU and PfKYNU complexes, respectively.

For HsKYNU complexes, hydrogen bonds formed with related residues in the active site throughout the simulations. However, there are also some hydrogen bonds that are unique to one of the complexes, highlighting differences in the specific interactions between substrates and enzymes. For example, the ring in 3-OH-KYN consistently

interacts with H102* and to faces the side chain of H102*, maintaining the binding conformation during MD simulations. (Figure 1A) In contrast, KYN fails to establish hydrogen bonds with H102*, resulting in an alternative binding conformation compared to 3-OH-KYN, as shown in Figure 3.1B. This distinct binding conformation is further supported by the presence of additional hydrogen bonds involving H253, K427, N429, Y275, N333*, and R428 in HsKYNU/KYN complex, which are not observed in the HsKYNU/3-OH-KYN complex (Table 3.1 and Figure 3.1B). Furthermore, when KYN adopts the inverted binding conformation relative to 3-OH-KYN, it binds outside the binding pocket and does not come back to the initial site.

On the other hand, for PfKYNU complexes, they showed stable binding conformations for both 3-OH-KYN and KYN during the simulations (Figure 3.2A and B). By following the same analysis done for HsKYNU complexes, we found the types of interacting residues in PfKYNU are quite similar to those in HsKYNU listed in **Table 3.1** although they are numbered differently (**Table 3.2**). However, PfKYNU/3-OH-KYN complex lacks certain hydrogen bonds due to the strong interactions between N- and C-terminus of 3-OH-KYN and PLP, causing the acidic group in 3-OH-KYN to be positioned further away from Y226, W256*, and T282*. The absence in hydrogen bonds in PfKYNU/KYN complex can be attributed to similar reason as mentioned earlier. The N- and C-termini of the substrate weakly interact with PLP, bringing them closer to Y226, T282*, and W256*, while being farther away from residues D33, N35, and H204. This is in contrast to PfKYNU/3-OH-KYN complex, which exhibits stronger interactions with PLP,

causing it to move away from residues Y226, T282*, and W256* and closer to residues on the opposite side, D33, N35, and H204, by making more interactions with additional polar hydroxyl group in its ring. Thus, the presence or absence of hydrogen bonds between the complexes is influenced by the strength of interaction with PLP, whether it is strong or relatively weak. Another notable difference is the involvement of R70*, which interacts with substrate' s ring and makes hydrogen bond. R70* demonstrates strong electrostatic properties in its amphipathic side chain, allowing it to form hydrogen bonds with the functional groups in ring in substrates. These hydrogen bonds were observed, regardless of whether the substrate is hydroxylated or not. Notably, the hydrogen bond populations were not found in monomer 1 of the PfKYNU/KYN complex, and we will further discuss about it in the next section.

Table 3.1. Hydrogen bond populations (>10%) in HsKYNU complexed with 3-OH-KYN and KYN during the simulations. Residues involved in hydrogen binding with symmetry-related monomer are marked with an asterisk mask (*).

Monomer	Enzyme residues	3-OH-KYN 〔%〕	KYN 〔%〕
Monomer 1	N74	68.0	51.0
	S75	43.0	36.2
	H102*	16.3	-
	E103*	17.5	-
	H253	-	18.5
	Y275	26.8	26.5
	PLP276	77.7	68.2
	D426	22.5	16.7
	K427	-	12.7
	R428	15.5	11.0
	N429	-	21.0
	R434	72.7	54.2
Monomer 2	N74	36.2	86.0
	S75	30.2	21.7
	H102*	11.7	-
	E103*	27.0	-
	H253	-	14.5
	Y275	43.8	-
	PLP276	83.2	90.3
	N333*	30.0	-
	D426	-	24.5
	R428	27.3	-
	R434	42.7	88.3

Table 3.2. Hydrogen bond populations (>10%) in PfKYNU complexed with 3-OH-KYN and KYN during the simulations. Residues involved in hydrogen binding with symmetry-related monomer are marked with an asterisk mask (*).

Monomer	Enzyme residues	3-OH-KYN 〔%〕	KYN 〔%〕
Monomer 1	D33	33.7	-
	N35	77.7	28.5
	S36	34.7	37.5
	R70*	15.7	15.3
	Y226	-	16.0
	PLP227	94.8	69.3
	D367	38.2	13.7
	R369	63.8	78.2
	R375	71.5	62.3
Monomer 2	D33	17.3	30.2
	N35	75.2	-
	S36	59.2	65.5
	R70*	-	15.8
	Y176	11.1	32.2
	H204	43.3	-
	Y226	29.8	53.5
	PLP227	99.8	45.8
	W256*	-	27.5
	T282*	-	30.0
	D367	29.0	56.3
	R369	68.0	66.2
	R375	97.5	24.5

Figure 3.1. Binding pocket of HsKYNU (orange cartoon) and the hydrogen bonding environment involving residues listed Table 1 when complexed with (A) 3-OH-KYN (cyan stick) and (B) KYN (magenta stick). The minimized (left) and final simulated structure at 200 ns (right) are exhibited. Hydrogen bonds formed between the side chain of H102* in HsKYNU and the functional groups in ring in substrates are indicated by red dashed arrow. (C) π-π stacking distance is shown as cyan and magenta dashed arrows for 3-OH-KYN and KYN, respectively. Distances over simulation time are represented for each monomer 1 (left) and monomer 2 (right).

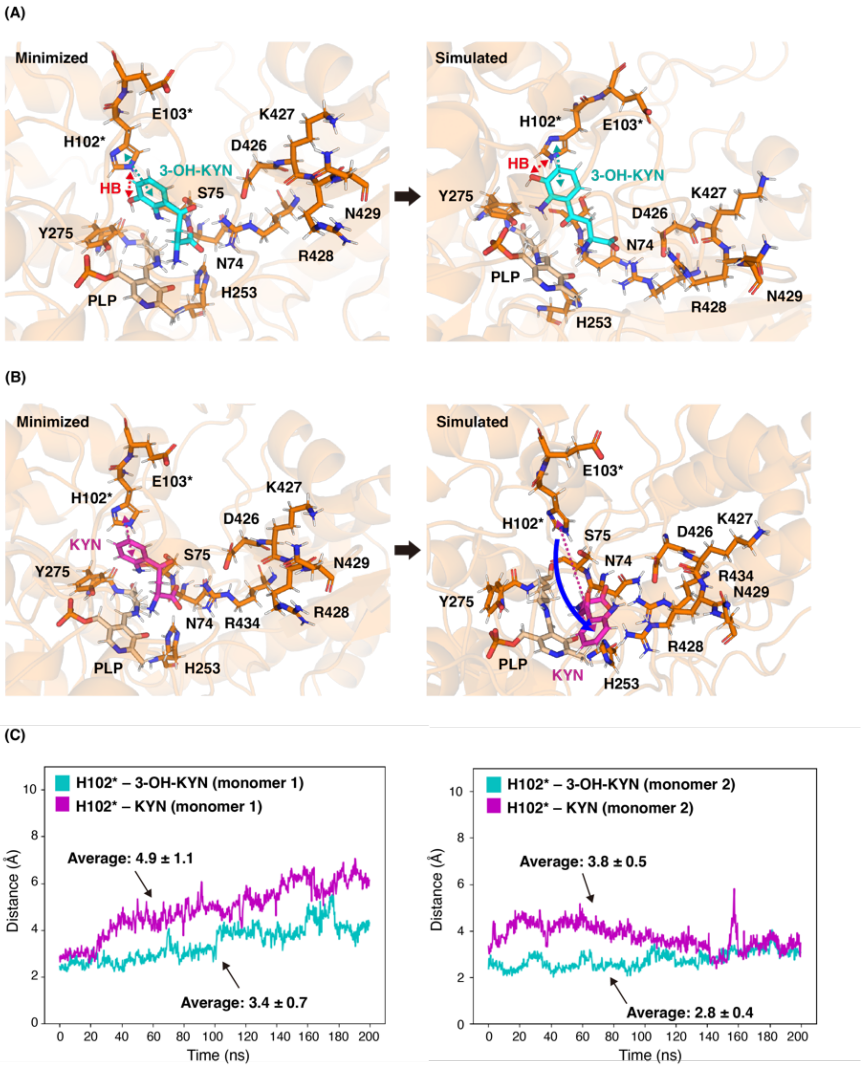

Figure 3.2. Binding pocket of PfKYNU (orange cartoon) and the hydrogen bonding environment involving residues listed Table 1 when complexed with (A) 3-OH-KYN (cyan stick) and (B) KYN (magenta stick). The minimized (left) and final simulated structure at 200 ns (right) are exhibited. Hydrogen bonds formed between the side chain of H102* in HsKYNU and the functional groups in ring in substrates are indicated by red dashed arrow. (C) π-cation stacking distance is shown as cyan and magenta dashed arrows for 3-OH-KYN and KYN, respectively. Distances over simulation time are represented for each monomer 1 (left) and monomer 2 (right).

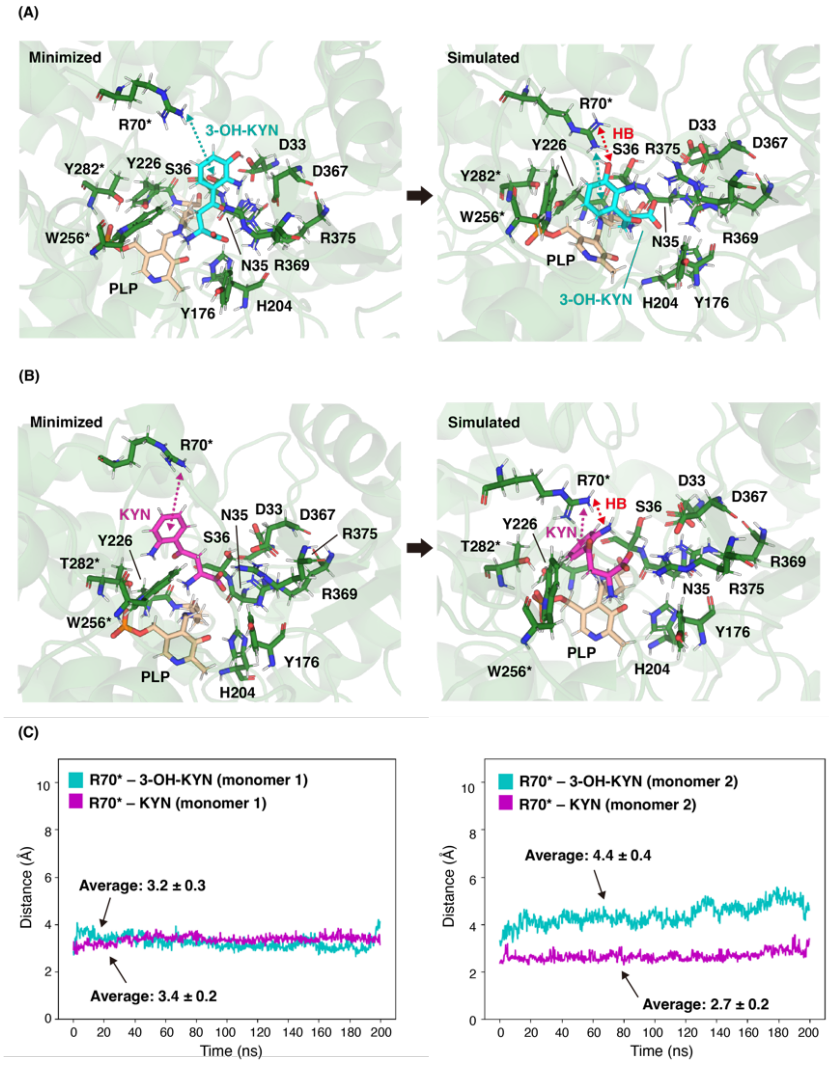

3.2.2. Impact of hydrogen bonds for mediating π-interactions

To access the potential impact of hydrogen bonds on **π-π** stacking interactions, we performed the analysis of time-dependent averaged **π-π** stacking distances between H102* and two substrates, 3-OH-KYN (cyan) and KYN (magenta), in each monomer (Figure 3.1C). Our results demonstrates that in all simulations, the average **π-π** stacking distances between H102* and 3-OH-KYN are 3.4 ± 0.7 Å for monomer 1 and 2.8 ± 0.4 Å for monomer 2 (cyan lines in Figure 3.1C left and right panel, respectively). In contrast, the average **π-π** stacking distances between H102* and KYN are 4.9 ± 1.1 Å for monomer 1 and 3.8 ± 0.5 Å for monomer 2, respectively (magenta lines in Figure 3.1C left and right panel, respectively). These results indicate that ring of KYN is positioned farther away from H102* and lacks strong interactions, such as hydrogen bond, due to the absence of hydroxyl group in its ring. Furthermore, the average distances of H102*−KYN steadily increase over the course of MD simulations, surpassing 3.5 Å threshold at around 12 ns (Figure 3.1C). This observation suggests that the ring of KYN exhibits weak interactions with H102*, leading to deviation from the initial binding conformation and flipped of KYN. In contrast, the hydrogen bonds formed between the hydroxyl group in the ring of 3-OH-KYN and the side chain of H102* play a crucial role in maintaing the **π-π** stacking interactions between them in HsKYNU/3-OH-KYN complex. Based on these findings, we propose that the presence of hydrogen bonds involving the hydroxyl group in the ring of 3-OH-KYN and the side chain of H102* is an important determinant for the higher catalytic efficiency exhibited by the HsKYNU/3-OH-KYN complex compared to the HsKYNU/KYN

complex.

We also analyzed **π** −cation distance formed between the protonated N in R70* and the center of mass of ring in substrates over simulation time (Figure 3.2C). To our delight, the populations of hydrogen bonds of R70* are in accordance with the present of **π**-cation interactions formed between substrates and R70* (Table 2 and Figure 3.2C). Concurrent with the hydrogen bond populations, the average **π**-cation distances in each symmetry-related monomers of PfKYNU complexes are below 3.5 Å – 3.2 ± 0.3 Å for monomer 1 in PfKYNU/3-OH-KYN, 3.4 ± 0.2 Å and 2.7 ± 0.2 Å for monomer 1 and 2 in PfKYNU/3-OH-KYN,respectively – except for monomer 1 of PfKYNU/KYN(4.4±0.4 Å) where hydrogen bonds with R70* are absent (Figure 3.2C). These hydrogen bonds formed with R70* may support to facilitate **π-π** stacking interactions between W64* and substrates, which are believed to be crucial for initiating the catalytic reactions, as suggested by Karamitros and co-workers. (Karamitros et al., 2020)

Evidently, by the multiple sequence alignment of KYNU family, Leucine in HsKYNU is at the equivalent position to R70* of PfKYNU. (Momany et. al., 2004) Leucin is insufficient to build strong interactions with substrates, regardless of whether they are hydroxylated or not. In a nutshell, the hydrogen bond is a pivotal interaction to have have substrates dominant binding pose for initiating the catalytic reactions and PfKYNU may easily be more accessible to both substrates than HsKYNU since R70* in PfKYNU can form the hydrogen bonds with any functional group in the ring in substrates by far-reached electrostatics.

3.3.3. Role of residence time in different catalytic activities of human and pseudomonas kynureninases

We extend our analysis to study the importance of hydrogen bonds formed between H102* and substrates in HsKYNU and R70* and substrates in PfKYNU. In doing so, we perform additional simulations of 100 ns repeated 50 times for each system, generating snapshots at 1 ns interval to store statistical data as mentioned earlier. By using the stored data trough MD trajectories, we calculate residence time of 3-OH-KYN and KYN in HsKYNU and PfKYNU by defining the bound and unbound states based on the π −interaction durations for 100 ns.

For HsKYNU, the **π-π** stacking interactions had an important role in fitting ring in the substrate to face with H102* which results in better catalytic efficiency (Figure 3.1). Therefore, if the distance between the center of mass of H102* and ring in substrates is below 4.5 Å in a given snapshot, it is considered as an **π-π** stacking interaction, and a residence time of 1 ns is added. Based on the residence time within a single trajectory, if it is less than 10 ns in both monomers, the complex in that trajectory is defined as unbound state, and as bound state if the residence time is equal to or greater than 10 ns (Figure 3.3). As can be seen in the orange pie chart in Figure 3.3, the HsKYNU has more number of bound states when making a complex with 3-OH-KYN, and the number of bound states is four times as much as the unbound states (bound : unbound = 40 : 10). On the other hand, HsKYNU/KYN complex exhibits a similar number of bound and unbound states, with a slightly higher number of unbound states (bound : unbound = 22 : 28). This result suggests

that HsKYNU has not a distinct preference to KYN, compared to 3-OH-KYN.

For PfKYNU, employing distance as a criterion, the time-dependent distance between the protonated N of R70* and the center of mass of ring in substrates are analyzed to determine the residence time and discern the bound or unbound states (Figure 3.4). In the green pie chart in Figure 3.4, PfKYNU complexes have more bound states regardless of the substrates (PfKYNU/3- OH-KYN; bound : unbound = 37 : 13, PfKYNU/KYN; bound : unbound = 46 : 4). This suggests that PfKYNU shows comparable preference for both 3-OH-KYN and KYN, indicating a lower substrates specificity compared to HSKYNU. These findings are consistent with the experimental K_D data, which reveals the PfKYNU/KYN complex exhibits approximately 13.3-fold higher binding affinity compared to HsKYNU/KYN and approximately 3-fold higher affinity than the HsKYNU/3-OH-KYN (Karamitros et al., 2020). In conclusion, our residence time calculations suggest that the **π-π** stacking between H102* in HsKYNU and ring in substrates, as well as **π**-cation stacking between R70* in PfKYNU and ring in substrates, may contribute to the disparity in catalytic efficiency observed between HsKYNU and PfKYNU towards 3-OH-KYN and KYN.

Figure 3.3. Histogram graph showing frequency of π-π stacking interactions between H102* in HsKYNU and ring in 3-OH-KYN (top, cyan bars) and KYN (bottom, magenta bars). The analysis involved 50 repeated calculations for each monomer 1 (darker bars) and monomer 2 (lighter bars), with each iteration producing 100 snapshots per 1 ns. The π-π stacking interactions are considered present when the π-π stacking distance is within 4.5 Å. The pie charts represent the distribution of bound (orange) and unbound (light orange) states across the 50 iterations. The unbound state is defined as interactions occurring withing 10 ns, while the bound state is defined as interactions lasting longer than 10 ns since we analyzed hydrogen bond populations more than 10 %.

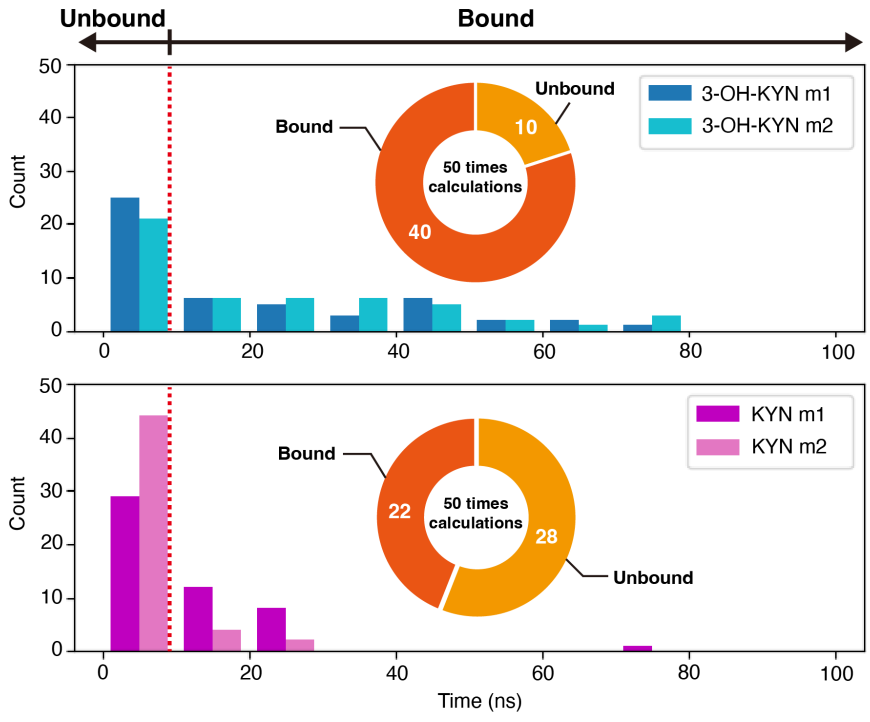

Figure 3.4. Histogram graph showing frequency of π-cation interactions between R70* in PfKYNU and ring in 3-OH-KYN (top, cyan bars) and KYN (bottom, magenta bars). The analysis involved 50 repeated calculations for each monomer 1 (darker bars) and monomer 2 (lighter bars), with each iteration producing 100 snapshots per 1 ns. The π-cation interactions are considered present when the π-cation distance is within 6.0 Å. The pie charts represent the distribution of bound (green) and unbound (light green) states across the 50 iterations. The unbound state is defined as interactions occurring withing 10 ns, while the bound state is defined as interactions lasting longer than 10 ns since we analyzed hydrogen bond populations more than 10 %.

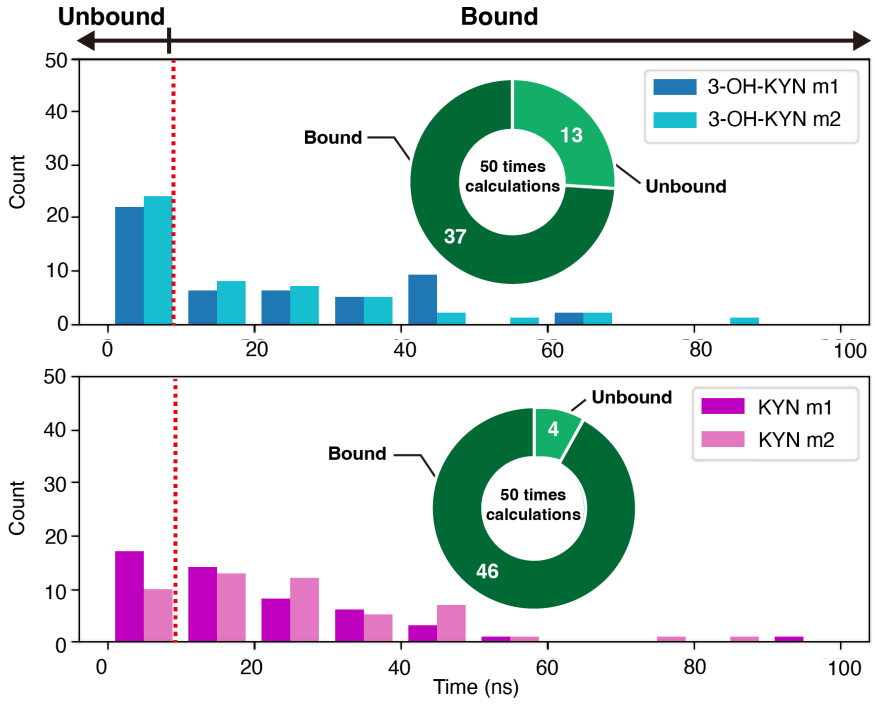

3.4. Conclusions

Understanding detailed atomic binding interactions between substrate and enzyme is essential for optimizing catalytic efficiency, and elucidating substrate selectivity in the atomic level has been challenging. In this study, we identified the populations of hydrogen bonds formed between substrates and enzyme residues and elucidated their role in maintaining the active conformation for higher catalytic activity. By employing all-atom MD simulations and residence time analysis, we investigated the molecular binding mechanism that underlies different enzyme kinetics. This study does not deal with the catalytic activity directly and handles only the process of substrate binding in terms of strength of binding and binding specificity. The insights gained from our research have the potential to facilitate the design of new humanized enzyme with enhanced catalytic efficiency.

4. CONCLUSION

In this thesis, we explored the thermodynamics and kinetics of functional proteins, SARS-CoV-2 neutralizing antibodies and candidates for therapeutic enzymes. First, we suggested thermodynamics methods to quantify the binding affinity of individual residues at the binding interface between SARS-CoV-2 RBD and its antibodies without introducing structural perturbations, enabling the assessment of their contributions to favorable binding. Next, we examined the binding interactions of two enzymes, originated from human and bacteria, when complexed with two distinct intermediates, 3-OH-KYN and KYN, in the kynurenine pathway.

Although our studies were based on the experimental findings, we conducted them through computational simulations and placed the focus on specific systems, and further investigations involving a broader range of systems would enhance our understanding of protein therapeutics. Despite these limitations, the knowledge gained from our works has the potential to contribute to the development of protein therapeutics. By elucidating the binding mechanisms in the view of thermodynamics and kinetics, we can better design and optimize therapeutic proteins to unravel the complexities of protein interactions and further advance the filed of protein therapeutics.

BIBLIOGRAPHY

KESKIN, O., GURSOY, A., MA, B. & NUSSINOV, R. 2008. Principles of protein-protein interactions: what are the preferred ways for proteins to interact? *Chem. Rev.*, 108, 1225-1244.

SUDHA, G., NUSSINOV, R. & SRINIVASAN, N. 2014. An overview of recent advances in structural bioinformatics of protein-protein interactions and a guide to their principles. *Prog. Biophys. Mol. Biol.*, 116, 141-150.

ZHU, J., AVAKYAN, N., KAKKIS, A., HOFFNAGLE, A. M., HAN, K. LI, Y., ZHANG, Z., CHOI, T. S., NA, Y., YU., C.-J. & TEZCAN, F. A. 2021. Protein assembly by design. *Chem. Rev.*, 121, 13701-13796.

LU, H., ZHOU, Q., HE, J., JIANG, Z., PENG, C., TONG, R. & SHI, J. 2020, Recent advances in the development of protein-protein interactions modulators: mechanisms and clinical trials. *Signal Transduct. Target. Ther.*, 5, 213.

GROMIHA, M. M., YUGANDHAR, K. & JEMIMAH, S. 2017. Protein-protein interactions: scoring schemes and binding affinity. *Curr. Opin. Struct. Biol.*, 44, 31-38.

DENG, Y. & ROUX, B. 2009. Computations of standard binding free energies with molecular dynamics simulations. *J. Phys. Chem. B.*, 113, 2234-2246.

BERNETTI, M., BERTAZZO, M. & MASETTI, M. 2020. Data-driven molecular dynamics: A multifaceted challenge. *Pharmaceuticals*, 13, 253.

BERTAZZO, M., GOBBO, D., DECHERCHI, S. & CAVALLI, A.

2021. Machine learning and enhanced sampling simulations for computing the potential of mean force and standard binding free energy. *J. Chem. Theory Comput.*, 17, 5287-5300.

VREVEN, T., HWANG, H., PIERCE, B. G. & WENG, Z. 2012. Prediction of protein-protein-binding free energies. *Protein Sci.*, 21, 396-404.

KOKH, D. B., AMARAL, M., BOMKE, J., GRÄDLER, U., MUSIL, D., BUCHSTALLER, H.-P., DREYER, M. K., FRECH, M., LOWINSKI, M., VALLEE, F., BIANCIOTTO, M., RAK, A. & WADE, R. C. 2018. Estimation of drug-target residence times by **τ**-random acceleration molecular dynamics simulations. *J. Chem. Theory Comput.*, 14, 3859-3869.

BERNETTI, M., MASETTI, M., ROCCHIA, W. & CAVALLI, A., 2019. Kinetics of drug binding and residence time. *Annu. Rev. Phys. Chem.*, 70, 143-171.

ARIKIN, M. R. & WELLS, J. A. 2004. Small-molecule inhibitors of protein-protein interactions: Progressing towards the dream. *Nat Rev Drug Discov.*, 3, 301–317.

SMITH, M. C. & GESTWICKI, J.E. 2012. Features of protein–protein interactions that translate into potent inhibitors: Topology, surface area and affinity. *Expert. Rev. Mol. Med.*, 14, E16.

PETTA, I., LIEVENS, S, LIBERT, C, TAVERNIER, J. & DE BOSSCHER, K. 2016. Modulation of protein–protein interactions for the development of novel therapeutics. *Mol. Ther.*, 24, 707–718.

SCOTT, D. E., BAYLY, A. R., ABELL, C. & SKIDMORE, J. 2016.

Small molecules, big targets: Drug discovery faces the protein–protein interaction challenge. *Nat. Rev. Drug. Discov.*, 15, 533–550.

MABONG, L. & KAPPO A. P. 2019. Protein–protein interaction modulators: Advances, successes and remaining challenges. *Biophys. Rev.*, 11, 559–581.

SIEBENMORGEN, T. & ZACHARIAS, M. 2020. Computational prediction of protein–protein binding affinities. *WIREs Comput. Mol. Sci.*, 10, e1448.

MOBLEY, D. L. & GILSON M. K. 2017. Predicting binding free energies: Frontiers and benchmarks. *Annu. Rev. Biophys.*, 46, 531–558.

GROMIHA, M. M., YUGANDHAR, K & JEMIMAH, S. 2017. Protein–protein interactions: Scoring schemes and binding affinity. *Curr. Opin. Struct. Biol.*, 44, 31–38.

VANGONE, A. & BONVIN, A.M. 2015. Contacts-based prediction of binding affinity in protein–protein complexes. *eLife*, 4, e07454.

RAO, V. SRINIVASA, K., SUJINI, G.N. & KUMAR G. N. S. 2014. Protein–protein interaction detection: Methods and analysis. *Int. J. Proteomics*. 2014, 147648.

MOREIRA, I. S., FERNANDES, P.A. & RAMOS M. J. 2007. Hot spots—a review of the protein–protein interface determinant amino-acid residues. *Proteins.*, 68, 803–812.

NERO, T.L. , MORTON, C. J., HOLIEN, J. K., WIELENS, J. &

PARKER, M. W. 2014. Oncogenic protein interfaces: Small molecules, big challenges. *Nat. Rev. Cancer.*, 14, 248 – 262.

MARCHAND, A., VAN HALL-BEAUVAIS, A. K. & CORREIA B. E. 2022. Computational design of novel protein- protein interactions — an overview on methodological approaches and applications. *Curr. Opin. Struct. Biol.*, 74, 102370.

CUNNINGHAM, B. C. & WELLS, J. A. 1989. High-resolution epitope mapping of hGH-receptor interactions by alanine-scanning mutagenesis. *Science.,* 244, 1081 – 1085.

KORTEMME, T., KIM, D. E. & BAKER D. 2004. Computational alanine scanning of protein – protein interfaces. *Sci. STKE.*, 219, pl2.

BOUKHARTA, L. & GUTÍERREZ-DE-TERÁNH, ÅQVIST, J. 2014. Computational prediction of alanine scanning and ligand binding energetics in G-protein coupled receptors. *PLOS Comput. Biol.,* 10, e1003585.

LIU, X., PENG, L., ZHOU, Y., ZHANG, Y. & ZHANG, J. Z. H. 2018. Computational alanine scanning with interaction entropy for protein – ligand binding free energies. *J. Chem. Theory. Comput.*, 14, 1772 – 1780.

MOREIRA, I. S., FERNANDES, P. A. & RAMOS, M. J. 2007. Computational alanine scanning mutagenesis— an improved methodological approach. *J. Comput. Chem.*, 28, 644 – 654.

SIMOES, I. C. M, COSTA, I. P. D, COIMBRA, J. T. S, RAMOS, M. J. & FERNANDES, P. A. 2017. New parameters for higher

accuracy in the computation of binding free energy differences upon alanine scanning mutagenesis on protein－protein interfaces. *J. Chem. Inf. Model.,* 57, 60－72.

DAVE, K., JAGER, M., NGUYEN, H., KELLY, J. W. & GRUEBELE, M. 2016. High-resolution mapping of the folding transition state of a WW domain. *J. Mol. Biol.*, 428, 1617－1636.

ARDEJANI, M. S., POWERS, E. T. & KELLY J. W. 2017. Using cooperatively folded peptides to measure interaction energies and conformational propensities. *Acc Chem Res.*, 50, 1875－1882.

LEE, J., SEOK, C., HAM, S. & CHONG, S. H. 2023. Atomic-level thermodynamics analysis of the binding free energy of SARS-CoV-2 neutralizing antibodies. *Proteins*. 91, 694-704.

GILSON, M. K., GIVEN, J. A., BUSH, B. L. & MCCAMMON, J. A. 1997. The statistical-thermodynamic basis for computation of binding affinities: A critical review. *Biophys. J.*, 72, 1047－1069.

LAZARIDIS, T. & KARPLUS, M. 1999. Effective energy function for proteins in solution. *Proteins.*, 35, 133－152.

LAZARIDIS, T. & KARPLUS, M. 2000. Effective energy functions for protein structure prediction. *Curr. Opin. Struct. Biol.*, 10, 139－145.

CHONG, S. H. & HAM, S. 2016. New computational approach for external entropy in protein－protein binding. *J. Chem. Theory. Comput.*, 12, 2509－2516.

GOHLKE, H. & CASE, D. A. 2004. Converging free energy estimates: MM-PB(GB)SA studies on the protein－protein complex Ras－Raf. *J. Comput. Chem.*, 25, 238－250.

BRYNGELSON, J. D., ONUCHIC, J. N., SOCCI, N. D. & WOLYNES, P. G. 1995. Funnels, pathways, and the energy landscape of protein folding: A synthesis. *Proteins.*, 21, 167 – 195.

CHONG, S. H. & HAM, S. 2011. Atomic decomposition of the protein solvation free energy and its application to amyloid-beta protein in water. *J. Chem. Phys.*, 135, 034506.

HURLBURT, N. K., SEYDOUX, E., WAN, Y. H, EDARA, V. V, STUART, A. B., FENG, J., SUTHAR, M. S., MCQUIRE, A. T., STAMATATOS, L. & PANCERA, M. 2020. Structural basis for potent neutralization of SARS-CoV-2 and role of antibody affinity maturation. *Nat. Commun.*, 11, 5413.

WU, Y., WANG, F., SHEN, C., PENG, W., LI, D., ZHAO, C., LI, Z., LI, S., BI, Y., YANG, Y., GONG, Y., XIAO, H., FAN, Z., TAN, S., WU, G., TAN, W., LU, X., FAN, C., WANG, Q., LIU, Y., ZHANG, C., QI, J., GAO, G.VF., GAO, F. & LIU, L. 2020. A noncompeting pair of human neutralizing antibodies block COVID-19 virus binding to its receptor ACE2. *Science*, 368, 1274 – 1278.

SHI, R., SHAN, C., DUAN, X., CHEN, Z., LIU, P., SONG, J., SONG, T., BI, X., HAN, C., WU, L., GAO, G., HU, X., ZHANG, Y., TONG, Z., HUANG, W., LIU, W. J., WU, G., ZHANG, B., WANG, L., QI, J., FENG, H., WANG, F. S., WANG, Q., GAO, G. F., YUAN, Z. & YAN, J. 2020. A human neutralizing antibody targets the receptor-binding site of SARS-CoV-2. *Nature*, 584, 120 – 124.

WEBB, B. & SALI, A. 2016. Comparative protein structure modeling using modeller. *Curr. Protoc. Bioinform.*, 54, 5.6.1.

CASE, D. A. et al. 2020. AMBER 20. University of California, San Francisco.

MAIER, J. A., MARTINEZ, C., KASAVAJHALA, K., WICKSTROM, L., HAUSER, K. E. & SIMMERLING, C. 2015. FF14SB: Improving the accuracy of protein side chain and backbone parameters from FF99SB. *J. Chem. Theory. Comput.*, 11, 3696–3713.

JORGENSEN, W. L., CHANDRASEKHAR, J., MADURA, J. D., IMPEY, R. W. & KLEIN, M. L. 1983. Comparison of simple potential functions for simulating liquid water. *J. Chem. Phys.*, 79, 926–935.

PASTOR, R. W., BROOKS, B. R. & SZABO, A. 1988. An analysis of the accuracy of Langevin and molecular dynamics algorithms. *Mol. Phys.*, 65, 1409–1419.

BERENDSEN, H. J. C., POSTMA, J. P. M., VAN GUNSTEREN, W. F, DINOLA, A. & HAAK, J. R. Molecular dynamics with coupling to an external bath. *J. Chem. Phys.*, 81, 3684–3690.

DARDEN, T., YORK, D. & PEDERSEN, L. 1993. Particle mesh Ewald: An N log N method for Ewald sums in large systems. *J. Chem. Phys.*, 98, 10089–10092.

IMAI, T., HARANO, Y., KINOSHITA, M., KOVALENKO, A. & HIRATA, F. 2006. A theoretical analysis on hydration thermodynamics of proteins. *J. Chem. Phys.*, 125, 024911.

KOVALENKO, A. 2003. Three-dimensional RISM theory for molecular liquids and solid-solid inter- faces. *In Molecular Theory of Solvation*, Hirata F, editor, 169–275, Kluwer Academic, Dordrecht

CHO, M. K., CHONG, S. H., SHIN, S., HAM, S. 2021. Thermodynamic stabilizing forces of the WW domain. *J. Phys. Chem. B.*, 125, 7108 – 7116.

CHOMG, S. H. & HAM, S. 2021. Time-dependent communication between multiple amino acids during protein folding. *Chem. Sci.*, 12, 5944 – 5951.

DILL, K. A. 1990. Dominant forces in protein folding. *Biochemistry*, 29, 7133 – 7155.

CHONG, S. H., IM, H. & HAM, S. 2019. Explicit characterization of the free energy landscape of pKID – KIX coupled folding and binding. *ACS Cent. Sci.*, 5, 1342 – 1351.

CHONG, S. H., HAM, S. 2019. Folding free energy landscape of ordered and intrinsically disordered proteins. *Sci. Rep.*, 9, 14927.

DIMITROV, D. S. 2012. Therapeutic proteins. *Methods Mol. Biol.*, 899, 1-26.

VELLARD, M. 2017. The enzyme as drug: application of enzymes as pharmaceuticals. *Curr. Opin. Biotechonol.*, 14, 444-450.

CHEN, R. 2001. Enzyme engineering: rational redesign versus directed evolution. *Trends. Biotechnol.,* 19, 13-14.

LI, X., ZHANG, Z. & SONG, J. 2012. Computational enzyme design approaches with significant biological outcomes: progress and challenges. *Struct. Biotechnol. J.*, 2, e201209007.

WELVORN, V. V. & HEAD-GORDON, T. 2019. Computational design of synthetic enzymes. *Chem. Rev.*, 119, 6613-6630.

MAZURENKO, S, PROKOP, Z & DAMBORSKY, J. 2020. Machine

learning in enzyme engineering. *ACS Catal.*, 10, 1210-1223.

FEEHAN, R., MONTEZANO, D. & SLUSKY, J. 2021. Machine learning for enzyme engineering, selection and design. *Protein Eng. Des. Sel.*, 34, gzab019.

KISS, G., RÖTHLISBERGER, D., BAKER, D. & HOUK, K. N. 2010. Evaluation and ranking of enzyme designs. *Protein Sci.*, 19, 1760-1773.

GARCÍA-GUEVARA, F., AVELAR, M., AYALA, M. & SEGOVIA, L. 2015. Computational tools applied to enzyme design – a review. *Biocatalysis*, 1, 109-117.

GROTTESI, A., BEŠKER, N., EMERSON, A., MANELFI, C., BECCARI, A. R., GRIGERIO, F., LINDAHI, E., CERCHIA, C. & TALARICO, C. 2020. Computational studies of SARS-CoV-2 3CLpro: insights from MD simulations. *Int. J. Mol. Sci.*, 21, 5346.

BUNZEL, H., ANDERSON, J. L., HILVERT, D., ARCUS V. L., KAMP, M. W. & MULHOLLAND, A. J. 2021, *Nat. Chem.*, 13, 1017-1022.

ROE, D. R. & CHEATHAM T. E. 2013. PTRAJ and CPPTRAJ: Software for processing and analysis of molecular dynamics trajectory data. *J. Chem. Theory Comput.*, 9, 3084-3095.

YANG, J., BAEK, M. & SEOK, C. 2019., GalaxyDock3: Protein-ligand docking that considers the full ligand conformational flexibility. *J. Comput. Chem.*, 40, 2739-2748.

KARAMITROS, C. S., MURRAY, K., SUGIYAMA, Y., KUMADA,

Y., JOHNSON, G., GEORGIOU, G., D' ARCY, S. & STONE, E. M. 2020. Conformational dynamics contribute to substrate selectivity and catalysis in human kynureninase. *ACS. Chem. Biol.*, 15, 3159-3166.

MOMANY, C., LEVDIKOV, L., BLAGOVA, S., LIMA, R. & PHILIPS, R. 2004. Three-Dimensional Structure of Kynureninase from Pseudomonas fluorescens, *Biochemistry*, 43, 1193-1203.

국문초록

생체 내에서 단백질의 동적 역할이 단백질 치료제 분야에서 매우 중요하게 다뤄지고 있다. 단백질은 다른 생물학적 경로를 방해하지 않으면서 면역 반응 유도, 생화학적 반응 촉매화, 분자 운송, 그리고 막단백질 형성 등 질병 완화에 특정하면서도 다양한 역할을 한다. 그러나 단백질-단백질과 단백질-리간드 상호작용에 대한 제한된 지식이 단백질 치료제의 발전을 어렵게 만든다.

본 논문에서는 항체나 효소와 같은 기능성 단백질의 분자 상호작용을 결합 열역학과 운동학의 관점에서 연구한다. 본 연구는 원자 단위의 분자동역학 시뮬레이션과 단백질 결합 구조의 잔기별 결합 자유 에너지 계산과 단백질에 결합된 리간드의 체류 시간 계산 결과를 통계적으로 분석하여 수행되었다. 먼저, 항체와 표적 단백질 사이에 동시에 다중의 상호작용이 형성될 때 결합 친화도가 좋아짐을 보인다. 그리고 효소 잔기와 리간드 사이에 형성되는 수소 결합에 의해 발생하는 **π**-상호작용이 안정적인 결합 구조를 유지하며, 이것이 효소와 리간드 결합 구조의 긴 체류 시간과 결합 운동학 향상에 영향을 미침을 보인다. 이러한 연구를 통해 우리는 단백질에서 일어나는 분자 상호작용에 대한 이해도를 높이고, 나아가 단백질 치료제 디자인 향상에 새로운 전략을 제시하는 데에 기여함을 목표로 한다.